

Effect of a Magnetic Field on the Synthesis of Single-Walled Carbon Nanotubes



Myriam Alexandre

Geophysical Science, University of Chicago

NNIN REU Site: Michigan Nanofabrication Facility, The University of Michigan Ann Arbor

NNIN REU Principal Investigator: Dr. Michael Keidar, Aerospace Engineering, University of Michigan Ann Arbor

NNIN REU Mentor: Tamir Arbel, Engineering, University of Michigan Ann Arbor

Contact: myriam@uchicago.edu, keidar@umich.edu, arbelt@umich.edu

Abstract

The full potential of carbon nanotubes for applications in engineering cannot be achieved until synthesis techniques are refined and methods to control nanotube characteristics are discovered. In this research project, the arc discharge method for producing single-walled carbon nanotubes (SWNTs) was used to test whether the addition of a magnetic field to the arc chamber will create longer SWNTs. Through analysis using scanning electron microscopy (SEM), samples taken from the arc chamber showed that, statistically, the average length of SWNTs produced with the magnetic field were longer than those produced without the addition of the magnetic field.

This suggests that with the addition of a magnetic field, the arc discharge method is an efficient and inexpensive method for producing longer SWNTs. From these results, it is predicted that increasing the magnitude will further increase the length of the SWNTs and produce more consistent results.

Introduction

SWNTs have extremely high tensile strength, elasticity, flexibility and high thermal conductivity. They can also be electrically conducting like metals or semiconducting depending on their structure; making them suitable for a wide range of applications from reinforcement material to microscale machinery. Several techniques have been developed for carbon nanotube synthesis. The most common methods are chemical vapor deposition (CVD) and arc discharge. These techniques are potentially viable as large-scale processes of producing SWNTs; however, they struggle with producing high quality, uniform and homogenous SWNTs that will hopefully make it easier to take advantage of the nanotubes' many potential applications.

CVD, at relatively low temperatures, uses a metal catalyst coated substrate in a heated chamber. Then two gases are introduced to the chamber; a process gas and a hydrocarbon gas. Its perk is that it does not require high temperatures, but the nanotubes it produces usually have defects in their structure. The arc discharge method involves the evaporation of a graphite anode filled with metal catalyst mixture by discharging an electric current between the electrodes. It offers poor flexibility and produces excessive amounts of unnecessary carbonaceous material.

In this research project, the arc discharge method for producing SWNTs is used to test whether the addition of a magnetic field to the arc chamber will affect the length of SWNTs. The theory behind adding the magnet predicts that if we can increase the density of the plasma between the electrodes, then we can

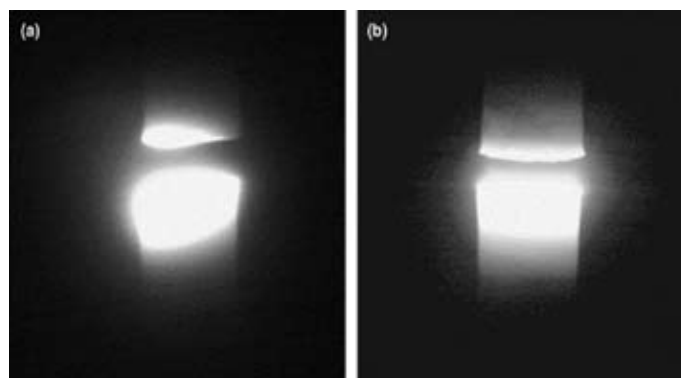
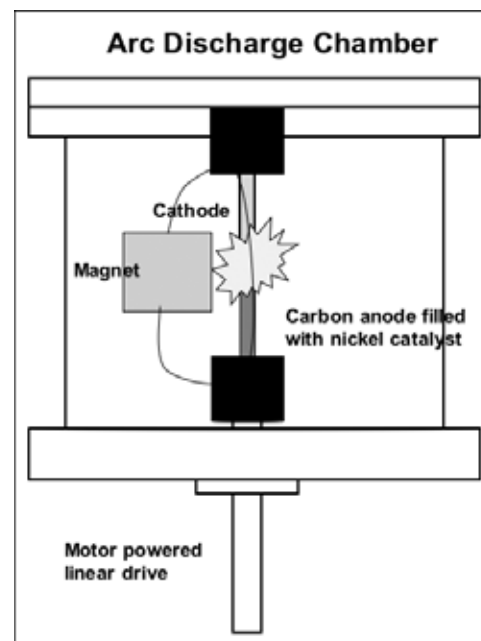


Figure 1: Photo of arc discharge; (a) without magnetic field, (b) with magnetic field.

increase the growth rate and consequently produce longer SWNTs. Adding the magnet has been shown to collimate the plasma in the chamber, specifically confining the plasma to the space between the electrodes and spreading it across the electrodes evenly as shown in Figure 1.

Experimental Procedure

We tested whether a magnetic field would make longer SWNTs by executing the arc discharge method of production with and without the magnet. The graphite anode was prepared by filling the 3" graphite rods with metal catalyst (Ni: Yt: C = 4:1: 95 %) and placing it in the chamber. Attached to the lid of the chamber was the stainless steel cathode. After the anode had been prepared, the lid was placed on the chamber. The chamber was vacuumed down and then pumped with helium at 650 Torr. The current that was sent between the electrodes was usually between 70 and 80 amps. While the current ran through the chamber, particles from the anode evaporated and condensed on the cathode and other regions of the chamber. As the anode shrank, the gap between the anode and the cathode was maintained by the chamber's motor-powered linear drive, thus maintaining the target current. The magnet was propped so that the magnetic field ran axially through both electrodes.

Samples from different regions of the chamber were collected. Samples from the deposit were found on a rod-like hard carbonaceous material that formed between the electrodes, and those taken from the collaret were found on material that formed above the cathode and around the deposit. Collected samples were analyzed under the SEM, which allowed us to take measurements of the SWNTs that were found.

Results and Discussion

Our SEM data indicated that the presence of a magnetic field made a significant difference in the average length of the SWNTs produced by the arc discharge method. Of the entire measurements taken without the magnetic field, 50% were under 600 nm and 90% were under 1300 nm; while 50% of the measurements taken from samples with the magnet were under 1100 nm and 90% were under 2600 nm.

Thus, the presence of the magnetic field seemingly doubled the length of the SWNTs produced. Additionally, samples from the deposit with magnetic field produced some of our longest SWNTs of over 6 μm in length. Hystograms are shown in Figure 2.

Conclusion

Our results indicate that, with the assistance of a magnetic field, the arc discharge method can consistently produce SWNTs of up to or over 6 μm in length. However, our main sources of error arise from limitations with the SEM. It only allows us to analyze a small area at a time and it severely lacks vertical resolution. Thus, there needs to be a more efficient and precise method of taking length measurements. Improving our understanding of SWNT formation and developing efficient techniques to disperse and purify the nanotubes will hopefully make our results more conclusive.

Acknowledgements

I would like to thank the National Nanotechnology Infrastructure Network Research Experience for Undergraduates Program, Intel Foundation, NSF, Sandrine Martin, and everyone else who has made this opportunity feasible. Your effort and contribution has been fruitful and has educated me about the endless research opportunities in nanotechnology. Thanks!

References

- [1] Keidar, M., "Modeling of the Anodic Arc Discharge and Conditions for Single-Wall Carbon Nanotube Growth." Journal of Nanoscience and Nanotechnology 2006.
- [2] Doherty S.P., "Semi-continuous production of multiwalled carbon nanotubes using magnetic field assisted arc furnace." Carbon 2005.

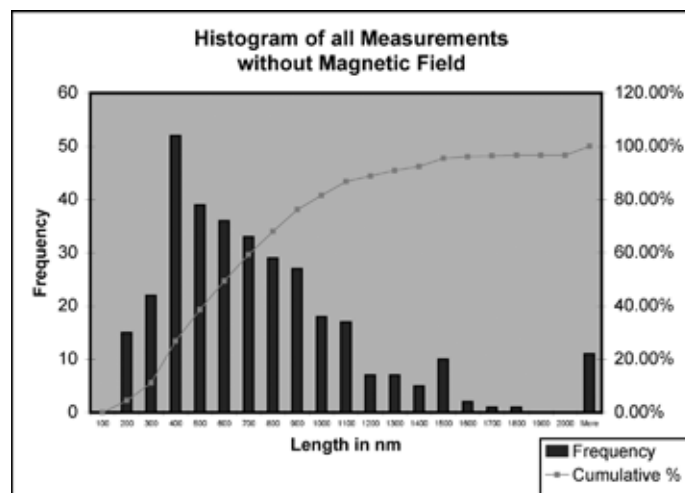
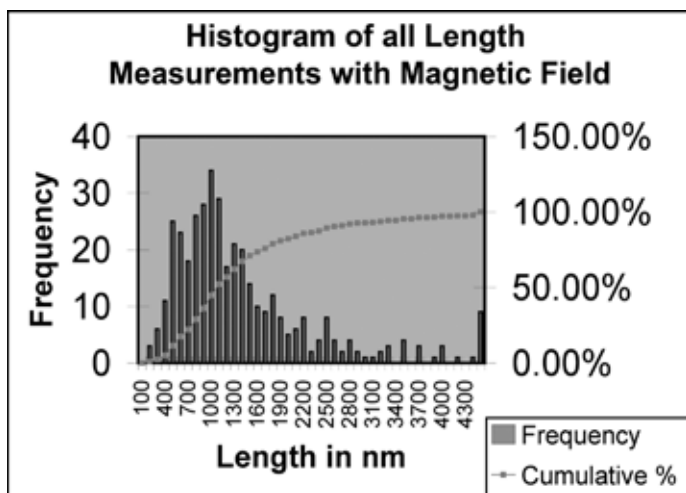


Figure 2

Nanowire Sensors

Andrea Boock

Engineering Science and Mechanics, The Pennsylvania State University at Altoona

NNIN REU Site: Penn State Center for Nanotechnology Education and Utilization, The Pennsylvania State University

NNIN REU Principal Investigator: Dr. Stephen J. Fonash, Center for Nanotechnology Education and Utilization, Pennsylvania State University

NNIN REU Mentor: Pilyeon Park, Materials Science and Engineering, Pennsylvania State University

Contact: aeb247@psu.edu, ppx908@psu.edu, fonash@engr.psu.edu

Abstract

The approach for growing nanowires (NWs) used here was the step-and-grow method, which combines the NW synthesizing and positioning step in an economic and safe way [1]. Template molds containing growth-controlling nanochannels were created with polydimethylsiloxane (PDMS) by using a master mold and placed over electrodes pre-positioned on a substrate. Polyaniline (PANI) NWs were then synthesized electrochemically in growth channels positioned between a biased anode and grounded cathode electrodes. The template molds could be stepped and the process repeated. After the synthesis of PANI NWs, they were tested for their sensitivity to humidity as a function of their surface to volume ratio. PANI NWs (110 nm) showed a linear response to humidity and could potentially function as a humidity sensor.

Introduction

Nanowires possess a high surface to volume ratio. This makes them excellent candidates for sensing applications, since a high surface to volume ratio improves detection sensitivity and response time due to more reaction area per volume and reduced diffusion time [2,3]. Most current approaches to growing nanowires require a synthesizing step, as well as a positioning step [4-6]. The overall approach for growth of the nanowires used here for sensing is the step-and-grow method, a novel approach that combines the two steps and eliminates the production of excess nanostructures [1].

Experimental Procedure

The first step was to create PDMS template molds using a previously created master mold. The master mold was made from a silicon wafer coated with 1 μm silicon dioxide, and was a positive image in relationship to the nanochannels, which would be created in the template mold. The template molds were created by spinning h-PDMS onto the master mold, curing at 65°C for 30 minutes, and adding s-PDMS mixture. They were then placed under vacuum, followed by a cure at 65°C for 3 hours. The template molds were then separated from the master molds and cut into rectangular slices with nanochannels located in the center of each piece.

The creation of the substrate began with patterning the electrodes onto a 2000Å silicon oxide coated Si wafer. The top surface of silicon oxide contained trenches patterned by dry etching and filled with platinum, with a titanium adhesion layer, deposited level with between the surface of the wafer.

In the synthesis of nanowires, the PDMS template molds were laid across the surface of the electrodes. An aniline monomer solution was then introduced to the opening of the nanochannels. 1V was applied to the anode by HP 4284a. PANI started to grow from the anode and filled the nanochannels until it reached to the grounded cathode. After carefully removing the PDMS template from the electrodes, PANI NWs are characterized by field emission scanning electron microscope (FESEM) and atomic force microscope (AFM). Figure 1 shows FESEM image of 111.6 nm PANI NW, and Figure 2 shows AFM image of the surface of PANI NW. Finally, PANI NW was tested for sensitivity to humidity, the results of which can be seen in Figure 3.

Results and Conclusions

Nanowire synthesis using the step-and-grow method is effective for synthesizing and positioning nanowires in a potentially economic manner. The PANI NWs were responsive to humidity and could potentially function as a humidity sensor.

Future Work

The step-and-grow approach can be used for synthesizing nanowires of many different materials. This opens up the opportunity for different types of nanowire sensors, as well as nanowire array structures.

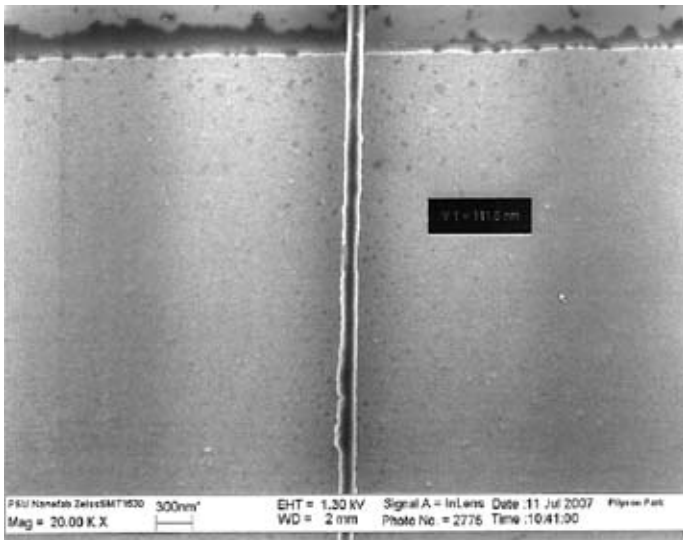


Figure 1: FESEM image of 111.6 nm polyaniline nanowire at 20.00 K X.

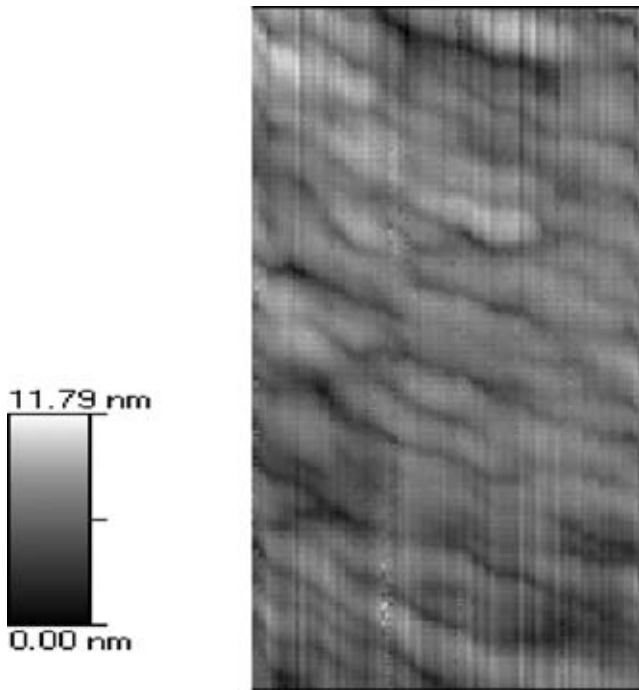


Figure 2: AFM image of polyaniline nanowire topology.

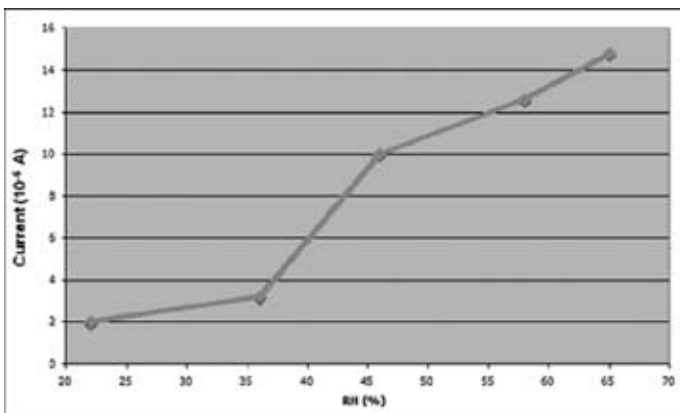


Figure 3: Relative humidity versus current when I V of electrical bias was applied to the device.

Acknowledgements

I would like to thank Pilyeon Park and Dr. Stephen J. Fonash for their support and guidance. Also, I am very grateful to the Penn State Nanofabrication Facility staff, as well as the staff of the Center for Nanotechnology Education and Utilization for a great experience. I would also like to thank the National Science Foundation and the National Nanotechnology Infrastructure Network REU Program for funding.

References

- [1] Nam, W. J, Carrion, H., Park, P., Garg, P., Joshi, S., Fonash, S. J., Proceedings of the 2007 International Manufacturing Science And Engineering Conference, 2007, Atlanta, Georgia, USA.
- [2] J. Huang, S. Virji, B. H. Weiller, and R. B. Kaner, Chem. Eur. J. 10, 1314 (2004).
- [3] D. Xie, Y. Jiang, W. Pan, D. Li, Z. Wu, and Y. Li, Sens. Actuators B, 81, 158 (2002).
- [4] L. Roschier, J. Pentilla, M. Martin, P. Hakonen, M. Paalanen, U. Tapper, E. I. Kauppinen, C. Journet, and P. Bernier, Appl. Phys. Lett. 75, 728 (1999).
- [5] Y. Huang, X. Duan, Q. Wei, and C. M. Lieber, Science, 291, 630 (2001).
- [6] P.A. Smith, C.D. Nordquist, T. N. Jackson, T. S. Mayer, B. R. Martin, J. Mbindyo, and T. E. Mallouk, Appl. Phys. Lett. 77, 1399 (2000).

Synthesis and Characterization of ZnO and PbI₂ Colloidal Nanoparticles

Shin Bowers

Biomedical Engineering, Brown University

NNIN REU Site: Nanoscience at the University of New Mexico

*NNIN Principal Investigator: Dr. Marek Osinski, Professor of Electrical and Computer Engineering,
Center for High Technology Materials, University of New Mexico*

*NNIN REU Mentor: Dr. Gennady Smolyakov, Research Asst Professor, Electrical & Computer Engineering,
Center for High Technology Materials, University of New Mexico*

Contact: shin_bowers@brown.edu, osinski@chtm.unm.edu, gen@chtm.unm.edu

Abstract

Many applications have been found for various nanocrystals. Specifically, zinc oxide (ZnO) can be used for various biomedical applications such as tissue imaging and deoxyribonucleic acid (DNA) detection while lead iodide (PbI₂) can be used as an x-ray detecting nanoscintillator. This project focused on the synthesis of quantum dots which emit in narrow spectral band for subsequent biomedical applications. ZnO was first synthesized by a low temperature colloidal process utilizing a Schlenk line set up. In an attempt to increase the intensity of the photoluminescence (PL) that the ZnO nanoparticles emit, the quantum dots were annealed at various temperatures and time intervals. PbI₂ was also synthesized through a low temperature colloidal process.

In order to characterize the nanoparticles, a spectrofluorometer was used to measure the excitation spectra. Low-temperature photoluminescence was measured using a closed-circuit helium cryostat and a helium-cadmium laser. Tunneling electron microscopy (TEM) and scanning electron microscopy (SEM) were performed to measure the size of the nanoparticles.

Experimental Procedure

ZnO was synthesized through a one-pot low temperature method utilizing a Schlenk line apparatus. First, 25 mL of *m*-xylene ($\geq 99.0\%$, Fluka) and 50 mL of 1-pentanol ($\geq 99.0\%$, Fluka) were added to a three-neck flask. Subsequently, 0.68g of *p*-toluene sulfonic acid (*p*-TSA) ($\geq 98.5\%$, Sigma-Aldrich) was added under the assumption of a decrease of spectral band width and increase of PL intensity [1]. The solution was stirred, and 2.5 g of zinc acetate dihydrate ($\geq 99.0\%$, Fluka) was added to the solution.

Under argon and reflux, the solution was heated for 1 hour and 20 minutes at 130°C and 1 mL aliquots were taken every 20 minutes. The solution was then centrifuged at 4000 rpm in 5 minute cycles with the addition of a 50% ethanol and deionized water stock solution until a white precipitate formed. The precipitate was diluted with ethanol and the solution was placed under vacuum until ZnO powder was obtained.

Annealing measurements for ZnO were conducted with a tube furnace. The ZnO powder was annealed at 200, 300, 400, and 500°C. At each temperature the powder was annealed in three 10 minute cycles. Cryostat measurements were conducted using a cold finger at decreasing temperatures up to 10 K.

PbI₂ was similarly synthesized through a low-temperature one-pot synthesis with a Schlenk line [2]. 100 mg of lead iodide powder ($\geq 99.999\%$, Aldrich) was dissolved in 15 mL of tetrahydrofuran (THF) ($\geq 99\%$, Sigma). The solution was sonicated until the powder was completely dispersed in the THF. The solution was

then centrifuged at 4000 rpms in 10 minute cycles until a deep yellow colored solution formed above a precipitate. The deep yellow colored solution was decanted into a three-neck flask.

10 mL of anhydrous methanol was injected into the solution under nitrogen and the solution was stirred at room temperature for 24 hours. 1 mL aliquots were taken at 10 minute, 1, 2, 4, and 8 hour intervals. 1 mg of dodecylamine ($\geq 98.0\%$, Fluka) was added to each aliquot immediately after it was taken. After 24 hours, the amount of solution inside the three-neck flask was measured and dodecylamine was added according to a 1 mg/mL ratio.

Results and Conclusions

ZnO synthesis was highly successful, producing nanoparticles that ranged from 4 to 10 nm. Figure 1 shows a 4 nm sized nanoparticle with parallel lines indicating the presence of a crystalline structure. The PL of the ZnO in Figure 2 shows the band-to-band emission of ZnO located at 380 nm, but also reveals a shoulder mound at longer wavelengths peaking at ~500 nm. In the cryogenic measurements under vacuum, as the temperature decreases, it is possible to see that this shoulder mound decreases in intensity, suggesting the possibility that this mound is caused by solvent-related defects on the surface of the ZnO. The annealing measurements (Figure 2) also showed this shoulder, and the ratio of shoulder to ZnO band-to-band emission decreased until 300°C.

Subsequent increases in temperature resulted in an increasing ratio, until the ZnO band-to-band emission was barely visible at 500°C. The ZnO sample at high annealing temperatures turned a dark charcoal color, indicating the possibility of carbon decomposition, the carbon possibly present from the solvents in the synthesis.

PbI₂ synthesis also proved to be highly successful. Figure 3 indicates that there is a distinct, narrow spectral range emitted from the lead iodide suggesting the presence of nanoparticles. Furthermore, the TEM in Figure 4 shows nanostructures on the range of 4 nm. The three differing parallel line structure present on the PbI₂ particle suggests that the crystal might be pyramidal in structure.

Future Work

Although distinct spectra existed for both ZnO and PbI₂, in order to increase PL intensity and minimize surface defect related PL, the particles will need to be coated. For subsequent biomedical applications, ZnO will need to be made water-soluble and bioconjugated. Water solubility will be achieved through the process of cap exchange, while bioconjugation will be made possible through the attachment of a protein layer. Finally, various tests and characterization methods must be conducted in order to prove the validity of these successive results.

Acknowledgements

I would like to thank Professor Marek Osinski and Dr. Gennady Smolyakov for their continual support and insight; Brian Akins, Tosifa Memon, and Krishnaprasad Sankar for their help with various syntheses; and Nathan Withers for the annealing experiments. Thanks to the National Nanotechnology Infrastructure Network Research Experience for Undergraduates Program, the National Science Foundation and the University of New Mexico for making this research experience possible.

References

- [1] Demir, M. M. et al.; "Precipitation of monodisperse ZnO nanocrystals via acid-catalyzed esterification of zinc acetate"; J. Mater. Chem. 28, 2940 (2006).
- [2] Finlayson, C. E. et al.; "Highly efficient blue photoluminescence from colloidal lead-iodide nanoparticles"; J. Phys. D-Appl. Phys. 39, 1477 (2006).

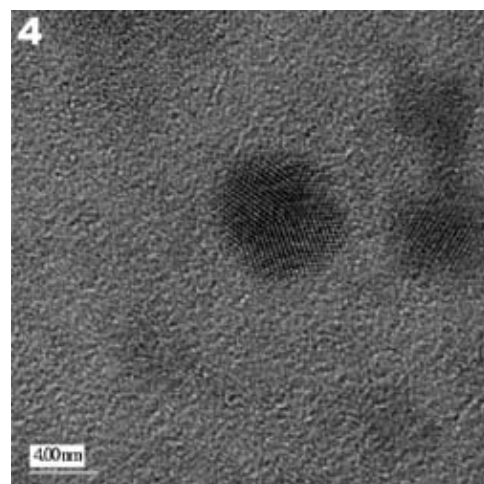
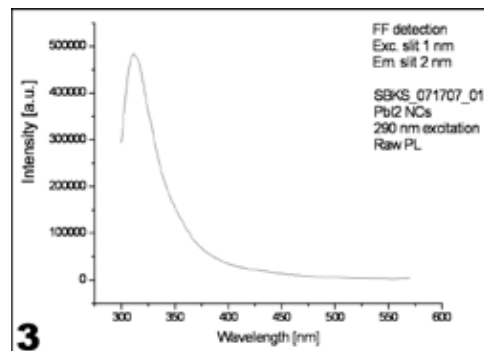
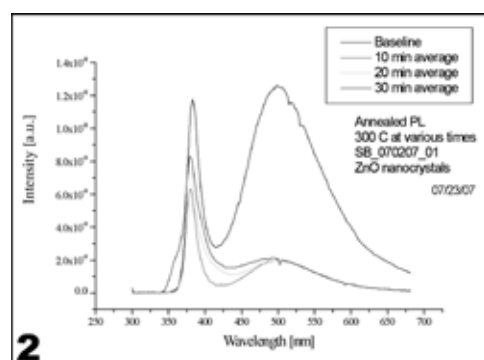
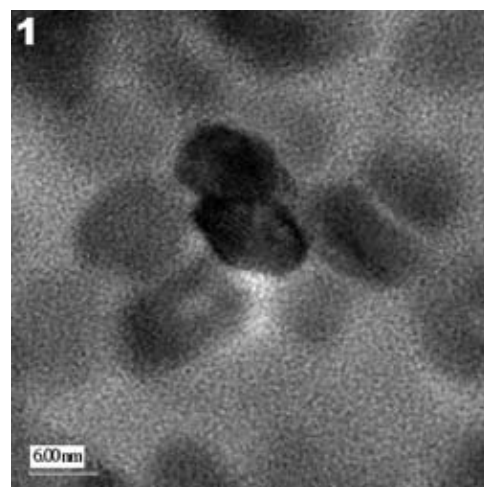


Figure 1, top: TEM image of ZnO nanoparticles.

Figure 2, upper middle: PL of ZnO annealed at 300°C for varying time intervals.

Figure 3, lower middle: PL of PbI₂ nanoparticles at 290 nm excitation.

Figure 4, bottom: TEM of PbI₂ nanoparticles.

Maskless Nanolithography Using an Atomic Force Microscope

Ian Frank

Physics, Pomona College

NNIN REU Site: Center for Nanoscale Systems, Harvard University

NNIN REU Principal Investigator: Prof. Marko Loncar, School of Engineering and Applied Sciences, Harvard University

NNIN REU Mentor: Dr. Jiangdong Deng, Center for Nanoscale Systems, Harvard University

Contact: ian.frank@pomona.edu loncar@seas.harvard.edu jdeng@cns.fas.harvard.edu

Abstract

We demonstrated possible applications for nanolithography using an atomic force microscope (AFM). We were able to anodically produce lines of aluminum oxide (AlO) on a thermally evaporated aluminum thin film by scanning the microscope tip across the substrate while applying a bias. Line widths < 70 nm were routinely obtained. A wet etch with phosphoric acid was shown to selectively etch the aluminum; leaving behind the aluminum oxide pattern creating what we hope will be an effective mask for reactive ion etching. We also demonstrated that this lithography method can be used to work with nanowires by drawing patterns near to and on top of zinc-oxide nanowires that had been coated with aluminum.

Introduction

Atomic force microscopy (AFM) nanolithography has been around for some time in various forms. The simplest method is merely scratching the surface of a substrate with the AFM tip. A more reproducible method, used in this work, is to create a bias between the tip and the surface while the AFM is in alternating current (AC) mode [1].

In AC mode, the AFM tip on the end of a cantilever is driven up and down at high-frequency and is not in contact with the surface, although it is within 5-10 nm of the surface. The result is an extremely high electric field between the sample and the tip which, combined with the water vapor in the air, anodically oxidizes certain surfaces. By optimizing the tip speed relative to the sample, the tip bias, and the tip-surface distance line widths as low as 10 nm on Al substrates have been reported [2].

AFM nanolithography is desirable for a number of reasons. Perhaps most importantly, the technology is far less expensive and more available than electron-beam lithography (EBL) and focused ion beam (FIB) milling technology which are the more traditional methods of achieving features of similar dimension. Beyond cost issues, AFM lithography is also advantageous over EBL and FIB because of its speed and relative simplicity.

Procedure

Our work was based mostly on the oxidation of aluminum thin films, though we made a few attempts to perform oxidation of silver layers as well. An important first step in achieving controlled oxidation on an aluminum substrate is to have as smooth a surface as possible. We optimized the operation conditions of thermal evaporation (TE) and yielded smooth Al surface with roughness less than 2 nm. Beyond having a smooth surface, we established that the substrate must be treated by

exposure to oxygen plasma immediately prior to the lithography. This treatment lasts for only a few hours and was essential for the success of the lithography. During the actual lithography, the best indicator of success was the tip being pulled into the surface. This could be easily monitored by watching the phase output of the AFM. If the phase dropped down into the attractive regime then oxidation of the substrate was almost certainly occurring.

Our Asylum Research AFM's internal power supply is limited to ± 10 V while literature suggests that the best results were obtained in the -12 to -30 V region [2]. Subsequently we built a circuit that would allow the AFM to turn an external power supply on and off at the appropriate times during the lithography. Once this circuit was in place, we noticed significant improvement in the contrast and quality of the oxidation lines we were able to produce on the aluminum.

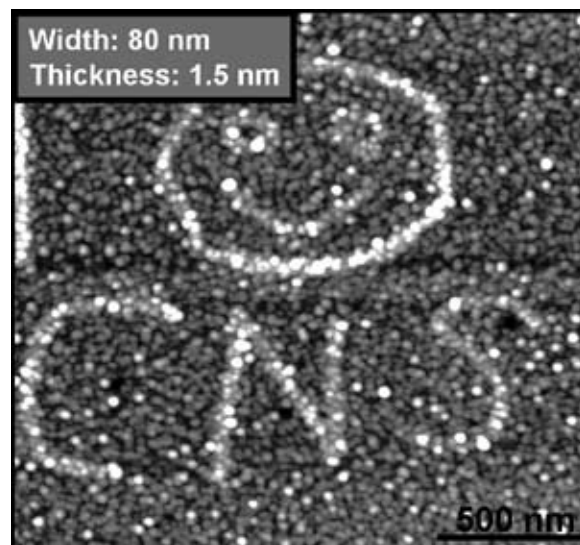


Figure 1

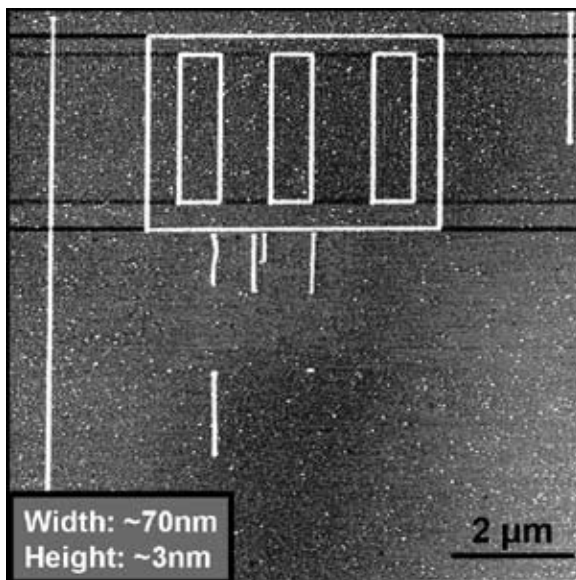


Figure 2

Figure 1 is an example of an oxide pattern drawn at -10 V. As you can see, the lines, while visible, are not solid and the pattern of the aluminum grains below are clearly visible. Figure 2 is an example of patterns drawn at -14 V with the help of the external power. These lines are more robust and solid.

Applications

Once oxidized, patterns were written on the aluminum substrate; a method for selectively removing either the aluminum or the oxide was required. This step was equivalent to the mask developing step in EBL for example. This would then allow the pattern to be transferred to the sample below the mask.

It was reported that phosphoric acid, diluted in deionized (DI) water, would very selectively etch the aluminum, leaving behind the aluminum oxide [1]. Figure 3 shows SEM images of three oxide lines on an aluminum thin film before and after the substrate was etched in phosphoric acid. As it can be seen, the contrast improves considerably in the right hand image as the lines go from being 3 nm thick to over 10 nm thick.

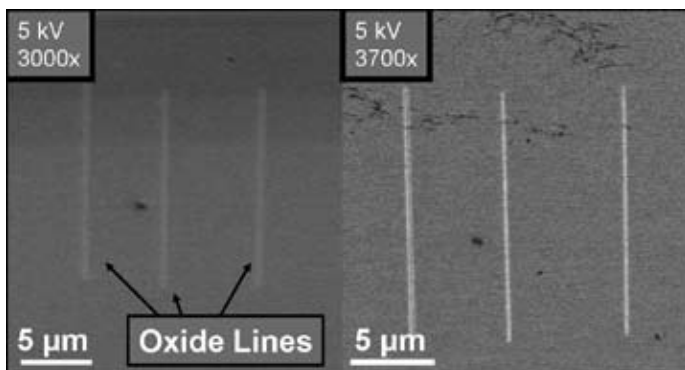


Figure 3

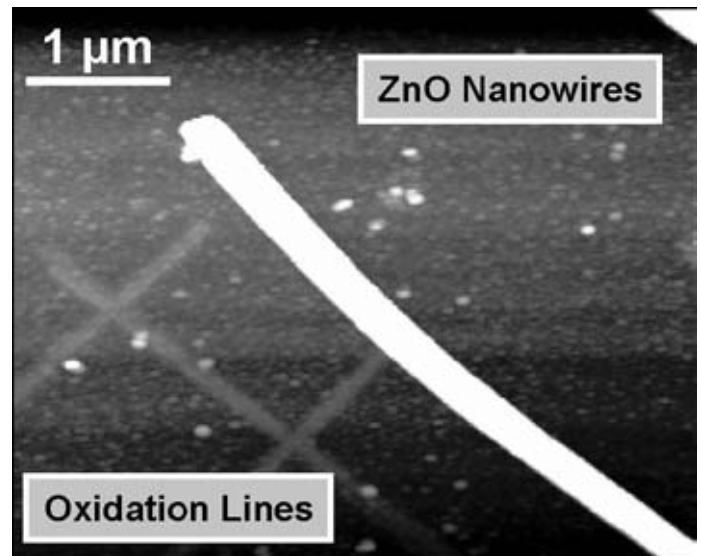


Figure 4

Figure 4 is an AFM image showing an example of oxide lines drawn around a zinc-oxide nanowire; demonstrating that this lithography technique can be used to create structures on and around nanowires. The dominating feature in the figure is the nanowire which is approximately 200 nm wide and 100 nm high. We believe that there is oxidation on top of the nanowire which is coated with aluminum; however, it is impossible to know with certainty due to the surface roughness and the color scale of the image.

Conclusions and Future Work

We demonstrated that AFM nanolithography can be a useful tool for cheaply and quickly creating RIE masks, as well as creating structures that will allow easier interaction with nanowires. We routinely achieved line widths < 70 nm, a number which promises to decrease as the process is optimized. Our future plans include using these demonstrated techniques to build working devices in the field of nano-optics. We are also attempting this technique on surfaces other than aluminum to allow for more diversity in the available applications.

Acknowledgements

I would like to thank Marko Loncar and J.D. Deng for their mentoring, Jim MacArthur for his help with electronic circuitry, and the NSF, National Nanotechnology Infrastructure Network Research Experience for Undergraduates Program and Center for Nanoscale Systems for their support.

References

- [1] Cochran, P., NNIN REU Research Accomplishments, 34 (2004).
- [2] Davis, Z.J. et Al. , Ultramicroscopy 97, 467 (2003).

Photo-CVD Coating of Nanoparticles with Silicon Dioxide

Brayden Glad

Mechanical Engineering and Materials Science, Duke University

NNIN REU Site: Minnesota Nanotechnology Cluster, University of Minnesota-Twin Cities

NNIN REU Principal Investigator: Dr. Steven Girshick, Mechanical Engineering, University of Minnesota-Twin Cities

NNIN REU Mentor: Adam Boies, Mechanical Engineering, University of Minnesota-Twin Cities

Contact: beg3@duke.edu, slg@umn.edu, aboies@me.umn.edu

Abstract

Extending previous research [1-6], the ability to coat nanoparticles with silicon dioxide (SiO_2) using a xenon (Xe_2) excimer lamp at standard atmospheric temperature and pressure was demonstrated using a photo-chemical vapor deposition (CVD) process. Sodium chloride (NaCl) was used as at the core particle, and tetraethyl orthosilicate (TEOS) in concentrations up to 0.70 sccm was provided as the SiO_2 precursor. NaCl particles of approximately 40-50 nm diameter received coatings of repeatable thickness after an exposure time of approximately 1 second in 172 nm light. The ability to control coating thickness by modifying TEOS flow rate was considered, and coating thickness was shown to increase with TEOS flow rate up to a maximum thickness of up to 2.0 nm in these conditions. Characterization showed the process provided a practically uniform covering of amorphous silica on approximately spherical particles.

Procedure

To verify the coating of particles, a straightforward tandem differential mobility analyzer setup (TDMA) was used. Sodium chloride, atomized with a nitrogen carrier gas, was dried and size selected using a differential mobility analyzer (DMA). Extra flow was vented to assure 1.0 slm through the DMA. The flow was mixed with varying quantities of tetraethyl orthosilicate (TEOS) with the appropriate amount of carrier nitrogen to maintain vapor pressure at the ambient 21°C.

The mixture then received 50 mW/cm² of 172 nm radiation from a Ushio UER20H-172C excimer lamp. Intensity was periodically verified using a Coherent Fieldmate laser power meter. A particle residence time in the illumination chamber of between 1.7-2.3 s was derived from an Ansys 10.0 flow simulation.

After receiving radiation, the aerosol passed through a charger, then a second DMA before entering a TSI 3025A condensation particle counter. Stepping through a range of voltages, the second DMA passed different mobility diameters to the counter, and provided a complete distribution of particles in the flow. Controls were created using the same setup with the lamp off, with TEOS varying between none and 0.70 sccm. To capture particles for characterization, electrostatic precipitation was used, with a voltage of 2.5 kV. For each collection, a standard Cu TEM grid was attached to the positive terminal of the precipitator. Additionally, for each collection used for the FTIR analysis, an uncharged stainless steel screen was placed directly across the flow path of the particles.

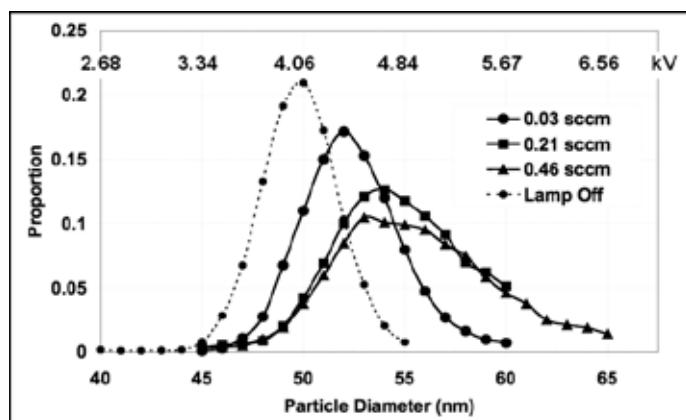


Figure 1: Mobility diameter by precursor quantity.

Results

The TDMA data demonstrate a size increase of the original particles as a result of the particle processing. Further TEM analysis indicates that the increased particle diameter is due to a coating process occurring as a result of photo-CVD. Both 40 and 50 nm particles experienced coating, however, most analysis was conducted on 50 nm particles because the atomizer produced a larger sample at that size.

In Figure 1, 50 nm particle results generated from the averages of five trials are presented. With increasing TEOS concentration, the particle coating thickness (half the difference between final and initial sizes) increased until a probable saturation thickness of about 2.0 nm. Thickness variation was approximately normally distributed, with more variance for larger TEOS flow rates. Tests without NaCl yielded minimal particles, implying that no self-nucleation of TEOS occurred.

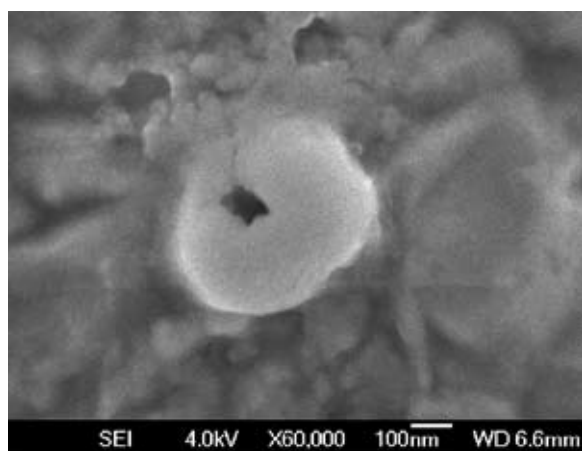


Figure 2: SEM image of an accumulation of coated nanoparticles.

Figure 2 displays a cluster of approximately spherical coated nanoparticles. There was evidence of some agglomeration, but individual particles of the appropriate size and consistent shape were clearly identifiable. This image was captured using a JEOL 6500 field transmission scanning electron microscope, operating with an excitation voltage of 4.0 kV, and a working distance of 6.6 mm. Figure 3, captured with a JEOL 1210 transmission electron microscope, clearly illustrates coatings of approximately uniform thickness despite a variety of vaguely spherical base particle shapes.

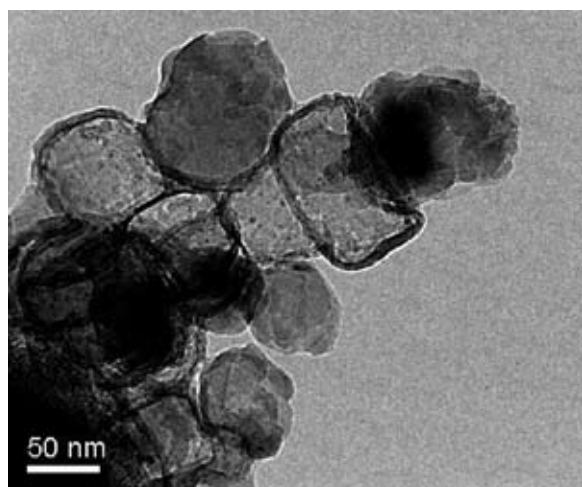


Figure 3: TEM image of nanoparticles and coatings.

X-ray diffraction characterization was conducted using a Bruker-AXS D5005, with a step size of 0.08 degrees 2- θ and 6.0 s step duration. Samples tested were polydisperse coated and uncoated particles, because no DMA was used. The results were analyzed using Jade 7.0, and no evidence of SiO₂ crystallization was found. Fourier-transform infrared radiation results were obtained with a Magma-IR 550 spectrometer.

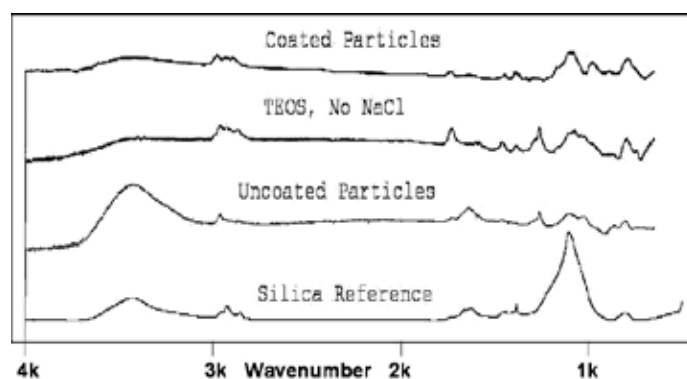


Figure 4: FTIR results.

Step size was 1 wave number with 30 samples per step, and the data was analyzed with Essential FTIR 1.20. Figure 4 shows that the difference between the coated particles and the uncoated control is only a few peaks, but each of those match a peak for silica, again providing strong evidence of coating. Particularly noticeable is the Si-O-Si asymmetric stretching peak at ~ 1120 wave number [5]. These silica peaks are more clearly pronounced in the coated particle data than the TEOS alone, demonstrating that the NaCl base contributes to silica formation.

Acknowledgements

We thank the Nitto Denko Corporation, the National Nanotechnology Infrastructure Network Research Experience for Undergraduates, and the National Science Foundation for material support. For their assistance on the project, Yuanqing He and Jami Hafiz also deserve thanks. Most importantly, I personally thank Dr. Steven Girshick, principal investigator, and Adam Boies, my mentor, for providing this opportunity.

References

- [1] Konuma, M; Film Deposition by Plasma Techniques; Springer-Verlag, Berlin (1992).
- [2] Kurosawa, K, et al.; "Silica Film Preparation by Chemical Vapor Deposition using Vacuum Ultraviolet Excimer Lamps"; Applied Surface Science, Vol. 168, pp. 37-40 (2000).
- [3] Lan, W, et al.; "Reaction Mechanism of Mercury-Sensitized Photochemical Vapor Deposited Silicon Oxide"; Japanese Journal of Applied Physics, Vol. 32 pp. 150-154 (1993).
- [4] Takezoe, N, et al.; "SiO₂ Thin Film Preparation using Dielectric Barrier Discharge-Driven Excimer Lamps"; Applied Surface Science, Vols. 138-139, pp. 340-343 (1999).
- [5] Yokotani, A, et al.; "Analysis of the Photochemical Reaction on the Surface for Room Temperature Deposition of SiO₂ Thin Films by Photo-CVD using Vacuum Ultraviolet Light"; Japanese Journal of Applied Physics, Vol. 44, pp. 1019-1021 (2005).
- [6] Zhang, B; "Growth of coatings on nanoparticles by photoinduced chemical vapor deposition"; Journal of Nanoparticle Research, online first, DOI: 10.1007/s11051-007-9238-2.

Controlling Fluid Flow to Conducting Polymer Biosensors Using Surface Modification



Thomas Gobert

Electrical and Electronic Engineering, McNeese State University

NNIN REU Site: Cornell NanoScale Science & Technology Facility, Cornell University

NNIN REU Principal Investigator: Prof. George Malliaras, Materials Science and Engineering, Cornell University

NNIN REU Mentor: John Defranco, Applied and Engineering Physics, Cornell University

Contact: t_gobert@yahoo.com, ggm1@cornell.edu, jad93@cornell.edu

Abstract

Fluorooctatrchlorosilane or FOTS, which is a hydrophobic monolayer (contact angle = 110°) that is used to modify substrate surfaces, is described for use in biosensor arrays. By lithographically patterning FOTS into arrays of hydrophilic channels with a hydrophobic background, confined passageways for fluid flow are created which allows a liquid sample to reach the sensing section of the substrate with low flow resistance. The sensor incorporates organic electrochemical transistors that are designed using poly(3,4-ethylenedioxythiophene) poly(styrenesulfonate) or PEDOT:PSS as the active layers for the gate and source-drain connections. This active layer represents the conducting polymer which interacts with the enzymatic ionic process and lowers the drain current depending on the concentration. The placement of deferent enzymes on each sensor in the array is used to measure the concentration of each unique parameter in the solution.

Introduction

Biosensors are used to detect and sense various materials, gases, and chemical compounds in an environment. The organic electrochemical biosensor that is used in this experiment senses for analytes in a chemical solution. Examples of such analytes are lactose, glucose, etc. A distribution array in order for different biosensors to sense unique analytes on the same platform has been designed using surface treatment techniques. This will enable users to detect multiple concentration levels at once and have micro-molar precision.

In previous designs, polydimethylsiloxane (PDMS) was used to control the fluid flow because of its barrier characteristics and simple fabrication methods. A technique that has been developed was to use a nanoscale monolayer as a surface treatment. This monolayer created a hydrophobic surface that could be placed anywhere on the surface.

Fabrication

The fabrication process consisted of developing two separate masks. The first mask had the fluidic pattern and the second mask had the source, drain, and gate placements for the multiple sensing sections. In order to fabricate the PEDOT:PSS connections, parylene has been coated on the silicon oxide wafer. The photolithographic process consisted of spinning SPR220-3.0 photoresist on the substrate and exposing it under the HTG System III-HR contact aligner for approximately 6 seconds. Before developing the substrate, it was placed in a 115°C heating plate for approx. 90 seconds. The substrate was developed using 30 MIF and then placed in the PlasmaTherm 72.

This process caused the exposed areas of the wafer to be etched away so that placement of the conducting polymer (PEDOT:PSS) could be placed. Acetone and IPA were used to rinse off the remaining photoresist so that the parylene could be the only layer left on the wafer. Spin-coating the PEDOT:PSS on the wafer allowed the polymer to fill in the patterns on the wafer. The parylene was then lifted off of the substrate by a peeling technique which only left the conducting layer. The substrate was then placed in a 120°C oven for 90 minutes. This process fabricated the source, drain, and gate onto the wafer.

The next process consisted of fabricating the distribution array of fluidic channels on the previously fabricated wafer. Again using the photo-lithographic techniques, the second mask was used to expose the fluidic channel regions onto the wafer. The wafer was developed using 300MIF and then was placed in the molecular vapor deposition tool, where it deposited a 5 nm hydrophobic layer of FOTS. Acetone and IPA was then used to remove the excess photoresist leaving only the outlined pattern and the connections hydrophilic.

Experimental Procedure

The substrates were tested by injected fluid via a syringe that held 40 ml. The fluidic channels were 3 mm in width and 5 mm in length. The fluid that was used to test the flow was de-ionized water. The water reached the testing sections effectively and enough fluid remained in the sensing area to test from. The PEDOT:PSS strips were tested for conductivity by using a voltmeter for ohmic resistance. By depositing an analyte as

the dielectric between the gate and source-drain electrodes, the biosensor was tested. Varying the gate voltage proved that the biosensor was functional because of the output drain current.

Results and Conclusions

The design enabled the surface-controlled fluid to flow with low resistance. Crosstalk between the channels was eliminated because of the hydrophobic gaps between the channels and the sensing sections. The multiple organic electro-chemical transistors were operable from the numerous fabrication processes and displayed functional voltage biasing.

Acknowledgements

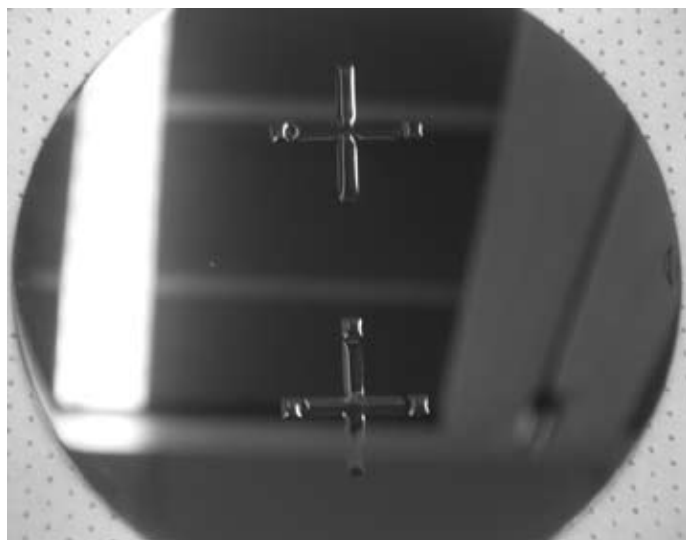
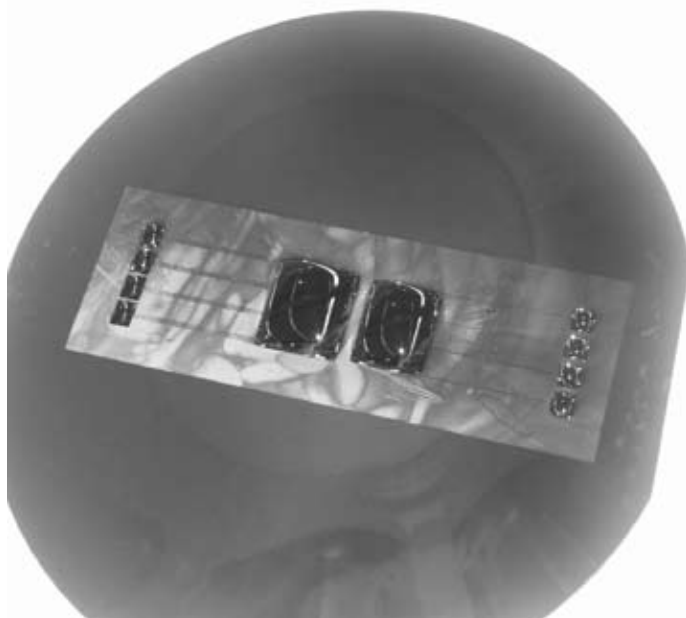
I would like to thank George Malliaras, J. A. Defranco, Melanie-Claire Mallison, and Lynn Rathbun. Special thanks to the Intel Foundation, National Nanotechnology Infrastructure Network Research Experience for Undergraduates Program, and National Science Foundation for funding.

References

- [1] J.T. Mabeck, J. A. Defranco, D. A. Bernards, and G. G. Malliaras, Applied Physics Letters 87, 013503 (2005).
- [2] J. A. Defranco, B. S. Schmidt, M. Lipson, G. G. Malliaras, Organic Electronics 7 (2006) 22-28.

Figure 1, top: Shows early design of fabricated substrate with 100 μm channels. The wafer has FOTS monolayer present which prohibits water-based solutions from adapting to the surface. The lightest area is covered with FOTS and the remaining is hydrophilic.

Figure 2, bottom: The design that worked best with the FOTS monolayer incorporated hydrophobic gaps that eliminated crosstalk between devices and the channel width allows fluid to flow with low resistance.



Synthesis of Palladium Nanoparticles for Methanol Steam Reforming Catalyst

Michael P. Johnson

Chemistry, Dana College

NNIN REU Site: Nanoscience at the University of New Mexico

NNIN REU Principal Investigator: Dr. Abhaya Datye, Center for Microengineered Materials, University of New Mexico

NNIN REU Mentor: Patrick D. Burton, Center for Microengineered Materials, University of New Mexico

Contact: mpjohnso@dana.edu, pburton@unm.edu, datye@unm.edu

Introduction

There is a need for energy in remote corners of the world. An energy storage technology is needed that can last longer than current batteries and is easily transportable. One possibility is to use hydrogen to power a fuel cell. However, the trouble with hydrogen is that it is hard to store and is also highly volatile. Our approach to hydrogen production and storage is through methanol steam reforming (MSR). Steam and methanol produce three moles of hydrogen and one mole of carbon dioxide. Methanol offers a high conversion rate and produces less by-products than other hydrocarbon fuels. The challenge is to make stable catalysts that work at low temperatures.

Current MSR catalysts are made of a copper/zinc oxide alloy and are active at 230°C. The problem is that these catalysts deactivate quickly. A palladium/zinc oxide (Pd/ZnO) catalyst offers the possibility of high methanol conversion over a longer time but is active at a higher temperatures and a greater mass of catalyst. Since catalysis is a surface phenomenon, the Pd/ZnO alloy can be made more active by increasing the surface area. The optimal particle diameter is 6 nm.

Experimental Procedure

Palladium acetate was reduced with octylamine in hexadecanediol at 270°C for 30 minutes. As the organometallic decomposed, Pd metal precipitated out of solution. During this process, the amines coated the surface of the Pd to protect against interparticle agglomeration. The Pd nanoparticles were washed in chloroform and methanol to remove excess amine ligands. The final product was a suspension of black nanoparticles in chloroform. The solution precipitation route was effective in synthesizing nanoparticles of Pd of ~ 4.5 nm in all samples as transmission electron microscopy (TEM) and scanning electron microscopy (SEM) reveal.

Once the Pd particles are synthesized, they were impregnated on a ZnO support to make a catalyst.

In order to preserve the morphology of the ZnO powder, it was necessary to use an organic medium rather than an acidic environment, as other methods use. The method for attaching the Pd to ZnO was to perform a ligand replacement on the Pd. 12-mercaptododecanoic acid was mixed into the suspension of nanoparticles for 10 minutes. A theoretical amount of 10% of the thiol/acid ligand was added based on the mass of the

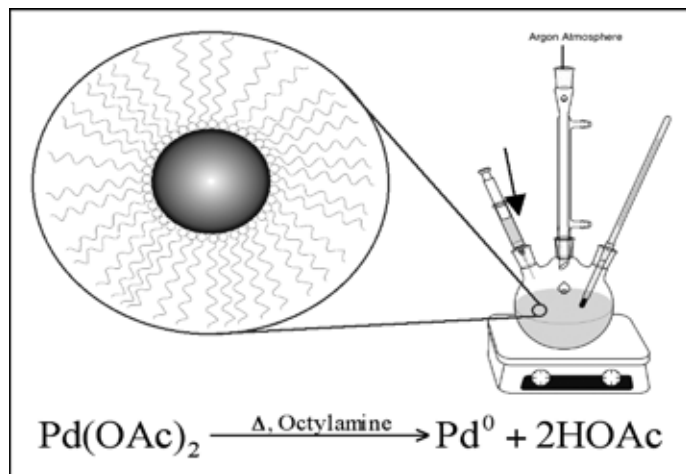


Figure 1: Solution precipitation.

nanoparticles. Infrared spectroscopy (IR) showed that a ligand substitution did take place. The theory of ligand substitution is that the thiol produces a stronger bond with Pd than an amine and the acid tail will bond with the surface of the ZnO. Pd will not agglomerate after amines are removed to reveal the Pd surface, because the particles will be anchored to the ZnO.

Problems in the synthesis came when depositing the Pd onto the ZnO surface. Several dispersion techniques were tested including incipient wetness, calcination at 80°C, mixing ZnO into the suspension, and a control of reducing palladium acetate on ZnO. (This is how the current Pd/ZnO alloys are formed.) The nanoparticles were prone to clump and form clusters rather than spread evenly onto the surface of ZnO.

Characterization

Pd decorated ZnO was partially formed. Spectroscopy measurements showed that ligand exchange took place. IR showed correct octylamine stretches before ligand replacement and clearly showed carboxylic acid stretches of the 12-mercaptododecanoic

acid after. X-ray diffraction showed that we had two crystalline phases of Pd and ZnO. Energy dispersive x-ray spectroscopy confirmed the composition.

Methanol is also capable of decomposing into hydrogen and carbon monoxide. Carbon monoxide (CO) binds to the Pd and deactivates the catalyst. However, this is not a problem as CO oxidation runs showed that the catalyst had a high selectivity to carbon dioxide (CO₂) over CO at reaction temperatures.

MSR was then performed on the catalysts. About 200 mg of catalyst was used in MSR and the average conversion was taken over four fifteen minute runs at 250°C. The control Pd/ZnO performed better because of the lack of ligands prohibiting the methanol interacting with the surface of the palladium. The best novel catalyst (Figure 2) had a methanol conversion of 41% and 35% selectivity towards CO₂. The best control catalyst was the 10% Pd:ZnO with 100% conversion and 87% selectivity.

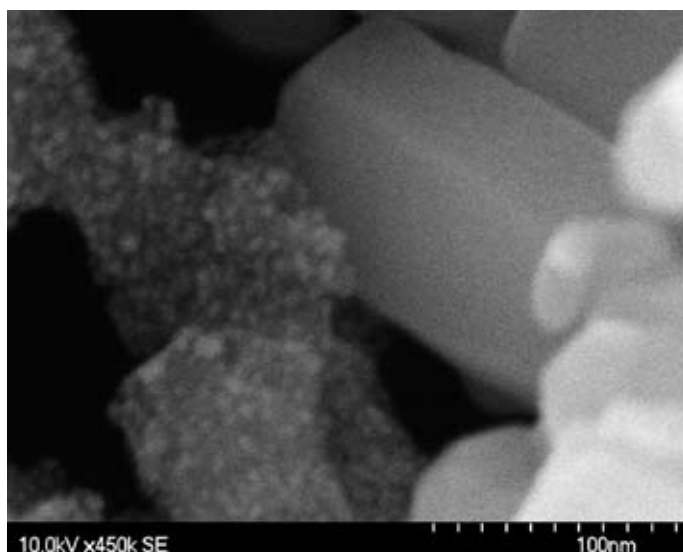


Figure 2: Pd/ZnO-incipient wetness.

Results

In this work, we have shown that it is possible to synthesize a catalyst from components of ligand-capped metal nanoparticles and metal oxide powders. The catalytic activity demonstrated by our catalysts using CO oxidation and MSR was low. The activity was hindered by residual ligands on the particles, resulting in a poor nanoparticle dispersion and overall powder coverage, as illustrated by TEM and SEM images.

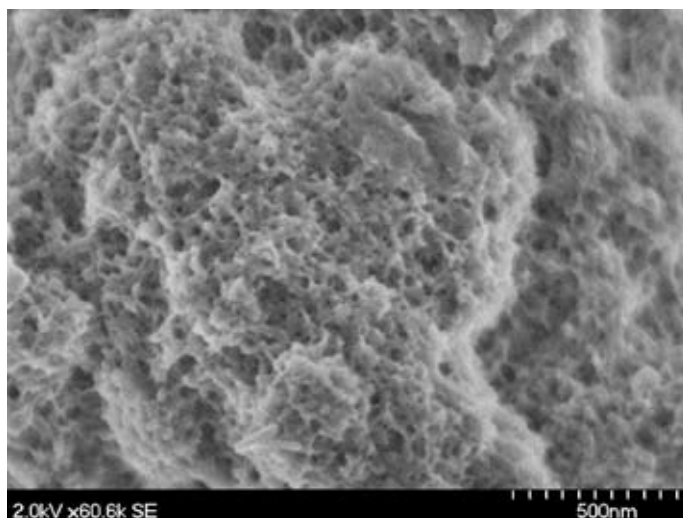


Figure 3: Pd/ZnO-ZnO doping.

Future Work

To improve our catalyst, it is necessary to enhance the particle dispersion over the oxide surface and remove excess ligands. Possible ways to coat the ZnO surface might be to functionalize the surface before adding nanoparticles or testing different ligands. Alternative deposition techniques also might need to be discovered. Even after coating with Pd, the amines need to be removed before any accurate MSR testing can occur. Possible techniques include an oxygen plasma etching process to gently remove excess amines. Although not yet perfect, this synthesis method offers a very promising way to collect hydrogen for fuel in the future.

Acknowledgments

I would like to send a personal thank-you to Patrick Burton and Timothy Boyle of the Advanced Materials Laboratory. I would also like to thank the National Science Foundation and the National Nanotechnology Infrastructure Network Research Experience for Undergraduates Program for granting me this amazing experience.

Sample (dispersion technique)	Methanol Conversion	Selectivity
2% Pd/ZnO (reduced on surface)	79%	90%
5% Pd/ZnO (reduced on surface)	5%	39%
8% Pd/ZnO (reduced on surface)	81%	95%
10% Pd/ZnO (reduced on surface)	100%	87%
15% Pd/ZnO (reduced on surface)	83%	96%
20% Pd/ZnO (reduced on surface)	75%	98%
Amine Coated Pd NPs (incipient wetness)	33%	53%
Thiol replaced Pd NPs (incipient wetness)	41%	35%
Thiol replaced Pd NPs (ZnO soaked in NP solution)	2%	37%

Figure 4: MSR conversion and selectivity.

Nanoimprinted Plasmonic Nanoparticles for Biosensor Applications



Emma Kamnang

Electrical Engineering, Corning Community College

NNIN REU Site: Michigan Nanofabrication Facility, University of Michigan Ann Arbor

NNIN REU Principal Investigator: Professor L. Jay Guo, Applied Physics; Engr. & Computer Science, University of Michigan

NNIN REU Mentor: Brandon D. Lucas, Applied Physics, University of Michigan

Contact: ekamnang@corning-cc.edu, emmacarole87@yahoo.com, guo@eecs.umich.edu, bdllucas@umich.edu

Abstract

Localized surface plasmon resonance (LSPR), free-electron density oscillations found in gold (Au) and silver (Ag) nanoparticle (NP) systems, has been studied extensively over the last decade in part because of the NP's ability to behave as nanoscopic transduction elements. In this study, metallic nanoparticle arrays (NPAs) were fabricated using the mold-based nanoimprint lithography (NIL) technique. The NIL approach, compared to other methods, allowed the complete control of the fabrication of nanopatterns possessing different sizes, shapes and interparticle spacing on a variety of substrates. The ability of these NPAs to transduce changes in their dielectric environment was exhibited through a controlled study using electron-beam deposited silicon dioxide (SiO_2). Additionally, the ability of these plasmonic NPAs to detect biological interactions was demonstrated using a high-affinity biotin-streptavidin model system.

Introduction

Surface plasmon resonance (SPR) biosensors have been utilized extensively to study biological interactions by monitoring changes in the resonance condition (i.e. critical angle and reflectance) of a suitably modified metal film. Similarly, its nanoparticle (NP) system analog known as localized surface plasmon resonance (LSPR) can be monitored using UV-Vis spectroscopy to transduce changes near the NP surface. These changes result in shifts of the resonance wavelength that is characterized by enhanced absorption and scattering of the NP system. Therefore, a suitably modified NP system offers the ability to also detect bimolecular interactions with commercially available spectroscopic systems.

Nanoparticle Array Fabrication

Glass substrates were first cleaned in a piranha solution, thoroughly rinsed with deionized water and dried using nitrogen (N_2). Nanoimprint resist was spin cast onto the substrates to achieve the appropriate film thickness and baked on a hot plate

to remove residual solvent. Imprinting was performed by heating the mold and substrate assembly above the resist glass transition temperature while in the imprint chamber, followed by an increase in the chamber pressure for approximately 5 minutes. The mold-substrate assembly was then cooled and separated to yield an imprinted pattern as shown in Figure 1. The final NP (Figure 1) was achieved by residual layer removal using oxygen (O_2) plasma reactive-ion etching (RIE), and Au electron-beam evaporation to the desired thickness and lift-off.

Experimental Methods

Extinction measurements of our fabricated NP system were accomplished through UV-Vis spectroscopy using a system comprised of an inverted microscope (Nikon TE300) and miniature spectrometer (Ocean Optics HR4000). In order to ascertain the distance-dependent dielectric response of Au NPAs possessing different height characteristics (40 nm; 60 nm; 80 nm),

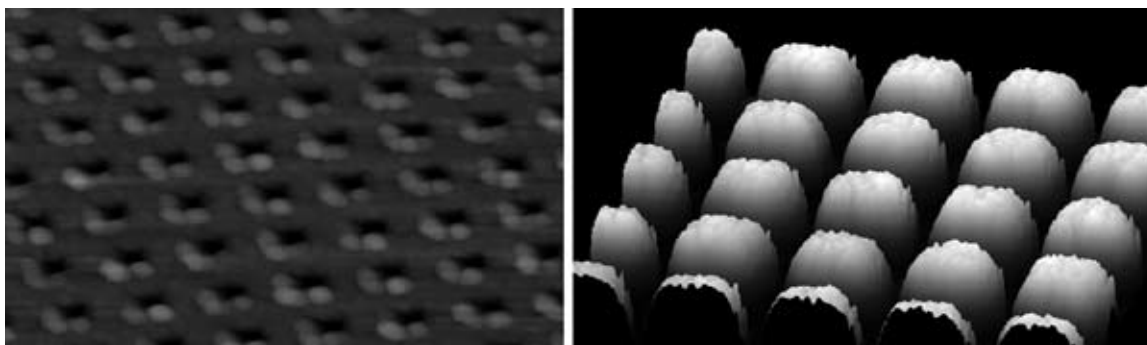


Figure 1: AFM images of imprinted sample and Au NPA.

evaporation of SiO₂ was performed to modify the dielectric environment of the NPA in a controlled manner. After ascertaining the initial resonance wavelength of the NPAs in ambient, extinction measurements were performed for multiple SiO₂ layer depositions on each NPA, iteratively.

Next, a Au NPA possessing a height of 40 nm was used to detect the specific binding interaction of a biotin-streptavidin system. This was accomplished by biotinylating the NPA through overnight incubation in a commercially available biotin-thiol self-assembled monolayer. The sample was incorporated into the experimental setup with a custom made flow cell that allowed increasing concentrations of streptavidin to flow across the biotinylated NPA surface using a peristaltic pump. Changes in LPR were acquired in real-time using data acquisition software. A standard commercially available SPR system was used as a control for the biological experiment.

Experimental Results

Figure 2 shows the resulting resonance shift due to changes in the SiO₂ layer thickness. It was found that the resonance peak amplitude, width and wavelength all increase with increasing SiO₂ layer thickness. Additionally, the 40 nm NPA was found to be the most sensitive to the SiO₂ layer thickness. All NPA systems also show a reduction in sensitivity as the oxide layer increases, and approach a saturated response. This demonstrates the ability of these NPAs to detect changes that occur only in the surrounding nano-environment. Figure 3 shows the ability of the NPAs to detect and monitor in real-time the specific binding of the biotin-streptavidin system. Each exposure of the biotinylated NPA to increasing streptavidin concentrations, followed by a wash in phosphate buffered solution to remove unbound streptavidin, were clearly observed for both the LSPR and SPR systems. The saturation of biotin binding sites with streptavidin was clearly observed through the saturated LSPR response which occurred much faster and at lower concentrations than found in the SPR system.

Conclusions

The ability of Au NPAs to detect changes in the local dielectric was exhibited using electron-beam evaporation of SiO₂. An increase in oxide film thickness caused an increase in the amplitude, width and wavelength of the LSPR. Shorter Au NPA constructs were found to be more sensitive to increases in oxide layer thickness. Additionally, all NPAs exhibited a reduction in their dielectric sensitivity with increasing oxide layer thickness and approached saturation. The relevance of these NPAs to biosensor applications was demonstrated through the detection of specific binding in a biotin-streptavidin system.

Acknowledgements

I would like to thank the National Science Foundation (NSF), Intel Foundation, Professor L. Jay Guo, Brandon Lucas, Dr. Vladimir Chegel, Dr. Sandrine Martin, Prof. Guo's research group, Michigan Nanofabrication Facility staff members, the National Nanotechnology Infrastructure Network Research Experiences for Undergraduates, and fellow NNIN REU 2007 interns at the MNF site for their help and support. Also, I would like to thank Professor Lawrence Josbeno for introducing me to the program.

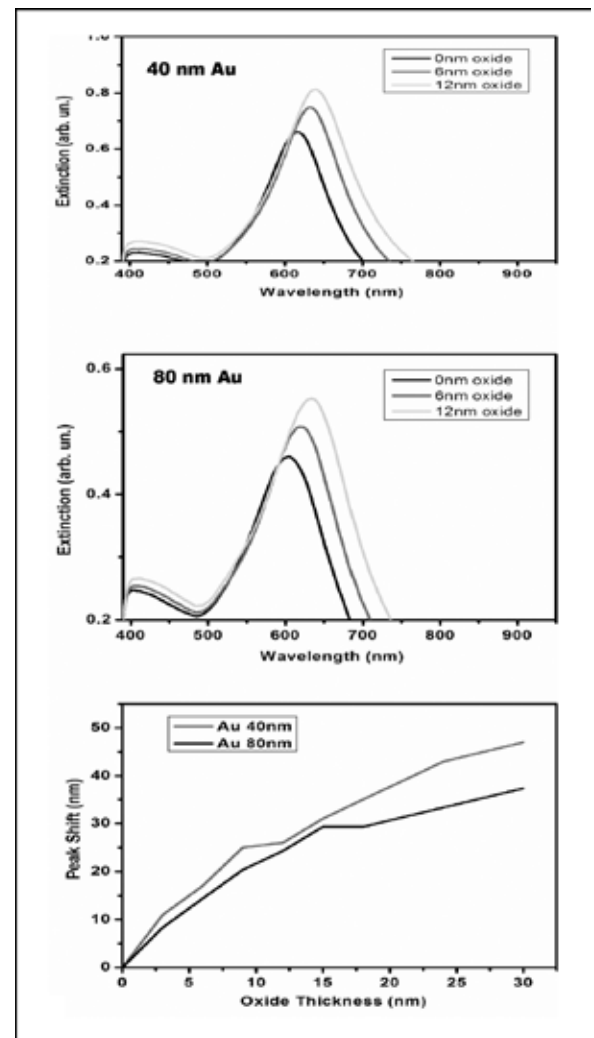


Figure 2: SiO₂ dielectric layer testing.

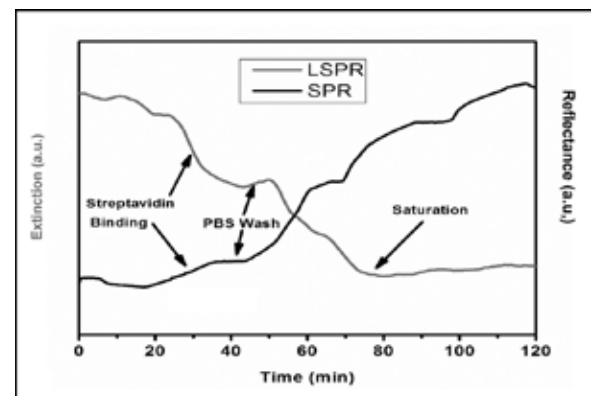


Figure 3: Streptavidin detection.

Use of Engineered Proteins for Organization of Nanostructures

Sarah Lee

Chemistry, Brigham Young University-Idaho

NNIN REU Site: Center for Nanotechnology, University of Washington

NNIN REU Principal Investigator: Beth A. Traxler, Microbiology, University of Washington

NNIN REU Mentors: Eliora Gachelet and Ruth Hall, Microbiology, University of Washington

Contact: lee04003@byui.edu, btraxler@u.washington.edu, gachelet@u.washington.edu

Abstract

The *Escherichia coli lac* repressor (LacI) is a deoxyribonucleic acid (DNA)-binding protein that regulates the production of proteins involved in lactose metabolism. Permissive sites within LacI have been previously identified, where short peptide sequences can be inserted without affecting the normal function of the protein. The sequence for the inorganic silica binding motif, QBP3, was inserted into a permissive site at residue 338 of the *E. coli lac* repressor, endowing LacI with the ability to bind both DNA and inorganic silica. After PCR screening for the QBP3 insert, six candidates were sequenced. Two were chosen for continued characterization. Western blot analysis of these constructs showed good protein expression, and β -galactosidase assays indicated LacI clones maintained normal function. The constructs showed some binding to fine silica and minimal binding to coarse silica. These analyses suggest the insertion at residue 338 binds less favorably to silica than the previously isolated QBP3 insertion at residue 317. Engineered proteins like these, that bind both DNA and inorganic compounds, can be utilized to arrange nanostructures in complex predictable patterns, using DNA as a scaffold.



Figure 1: Diagram describing the function of the lac repressor (LacI).

Introduction

The expression of proteins involved in lactose metabolism in *Escherichia coli* are regulated by the DNA-binding protein lac repressor (LacI). LacI normally functions as a tetramer which binds to the lac operator (Figure 1). RNA polymerase binding is inhibited, repressing lac transcription and protein production. In the presence of lactose, allolactose binds to the tetramer inducing a conformational change. This new shape cannot bind to the lac operator, so transcription of the lactose metabolism genes occurs. Permissive sites have been previously identified within LacI [1]. These sites are permissive because short sequences can be inserted there without affecting the normal function of the protein. QBP3, a known amino acid sequence with the ability to bind silica [2], was inserted into the permissive site at residue

338 of LacI, endowing LacI with the ability to bind both DNA and silica. Expression, function and silica binding capability of the Lac-I derivatives were characterized.

Proteins with this dual binding ability can use DNA as a scaffold to organize nanostructures in complex predictable patterns. As more proteins are engineered to bind DNA and inorganic compounds, organization of complex nanostructures will become a more efficient process.

Experimental Procedure:

Construction of LacI-338::QBP3

A plasmid with the lacI-338::i31 gene, *placI-338::i31* [1], was used as a cloning vector and digested with the restriction enzyme BamHI. The coding sequence for the silica binding motif, QBP3 (Leu-Pro-Asp-Trp-Trp-Pro-Pro-Gln-Leu-Tyr-His), was PCR amplified using engineered primers (5'TTCGCAATTCCTTTAGATCTACCTTTCTATTCTCACTCT3' and 5'ACTTTCAACAGTTTCGGCCAGATCT CCA CC3') which were designed to amplify the QBP3 coding sequence and introduce BglIII restriction sites. The PCR product was purified via ethanol precipitation and digested with BglIII. BglIII and BamHI restriction sites leave identical overhangs which facilitated the ligation of QBP3 and *plac-338::i31*. To minimize ligation of the vector without the QBP3 insert, a background BamHI digest followed the ligation. Reactions were transformed into DH5 α competent *E. coli* and plated onto LB plates, supplemented with 100 μ g/ml ampicillin, and incubated overnight at 37°C.

90 reactions were screened by PCR with the engineered primers QBPINT and 3'LacIR, which bind within and downstream of the QBP3 insert. Six candidates were further screened by sequencing. QBP3 contains a BseRI restriction site not present

in the vector. Two candidates were cut with BseRI to confirm the insertion, and chosen for further characterization (denoted 29 and 38 in the figures).

Characterization of LacI-338::QBP3

Protein expression of the clones was determined by western blotting, using the monoclonal anti-LacI primary antibody. β -galactosidase assays were carried out as described by Kleina and Miller [3] to determine DNA binding activity, in high and low plasmid copy number *E. coli* strains, CSH140 and BN29, respectively.

Silica binding assays were done with cell extracts containing various LacI derivatives supplemented with fine or coarse silica powders. Assays were incubated for 10 minutes with rotation at room temperature, then harvested. The ability of protein to bind to silica (indicated by fractionation to the pellets) was measured. Protein was detected using the LacI antibody on a Western blot.

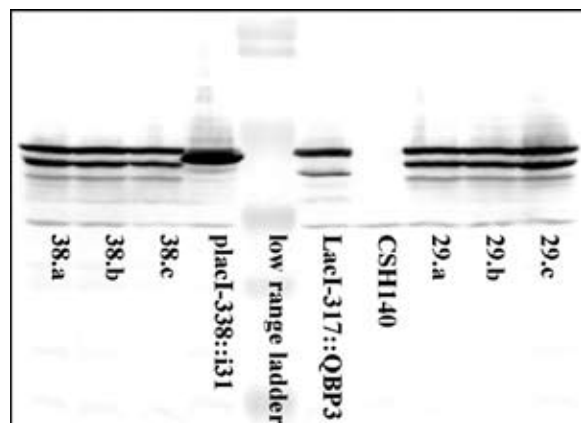


Figure 2: Western blot analysis of protein expression.

Results and Conclusions

Two LacI-338::QBP3 clones were isolated and characterized. The LacI-338::QBP3 derivatives displayed good protein expression [Figure 2]. Smaller LacI-related bands were present in the Western blot, suggesting these proteins were somewhat more susceptible to degradation than the positive controls. β -galactosidase assays showed good repression activity was maintained in both strains, indicating DNA binding by LacI-338::QBP3 (Table 1). The clones displayed some fine silica binding and even less affinity for coarse silica (Figure 3). The silica binding assays also suggested the insertion at residue 338 binds less favorably to silica than the insertion at residue 317.

Future Work

It will be of interest to determine whether the affinity for binding various inorganic compounds varies by motif insertion at different locations, as seen here. Also, this project can be continued with the characterization of QBP3 and other inorganic binding sequence inserts into various DNA-binding proteins.

As more constructs are built and characterized, organization of nanostructures using these engineered proteins will become a more efficient process.

Acknowledgments

The National Nanotechnology Infrastructure Network Research Experience for Undergraduates Program and the National Science Foundation. Special thanks to Beth Traxler, Eliora Gachelet, Ruth Hall and Rembrandt Haft.

References

- [1] Nelson, B.; C. Manoil; B. Traxler; J. Bacteriol., 179, 3721-28 (1997).
- [2] Oren, E.E.; C. Tamerler; D. Sahin; M. Hnilova; U.O.S. Seker; M. Sarikaya; R. Samudrala; Bioinformatics, (2007), in press.
- [3] Kleina, L. G.; Miller, J. H.; J. Mol. Biol., 212, 295-318 (1990).

mutant	β -gal activity
(assayed in CSH140)	
pTrc99A (wt LacI)	0.0010
LacI-317::QBP3	0.0003
placi-338::i31	0.0005
29.a	0.0007
29.b	0.0008
29.c	0.0009
38.a	0.0006
38.b	0.0008
38.c	0.0006
(assayed in BN29)	
BN29	152.863
pTrc99A (wt LacI)	0.598
placi-338::i31	7.200
29.a	17.300
38.c	10.39

Table 1: β -galactosidase activity in Miller units.

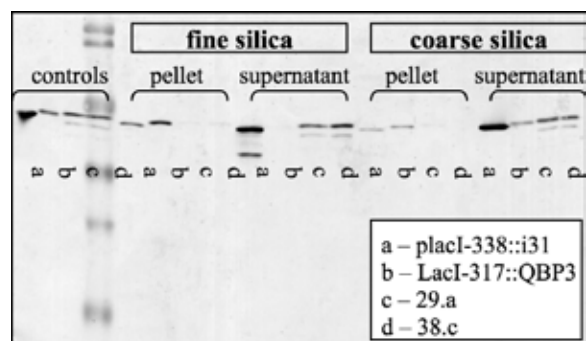


Figure 3: Western blot analysis of silica binding assays.

Atomic Force Microscopy Grain Structure Characterization of Perpendicular Magnetic Recording Media

Alexander Luce

Engineering Physics, University of Arizona

NNIN REU Site: Stanford Nanofabrication Facility, Stanford University

NNIN REU Principal Investigator: Professor Robert Sinclair, Materials Science and Engineering, Stanford University

NNIN REU Mentor: Faraz Hossein-Babaei, Department of Materials Science and Engineering, Stanford University

Contact: aluce@email.arizona.edu, bobsinc@stanford.edu, farazhb@stanford.edu

Abstract

Magnetic recording technology plays a key role in the development of computer, audio, and video storage devices. The nanoscale grain size of current hard-disk media determines important recording properties and thus requires accurate characterization methods. In this work, we developed a new method to characterize the nanostructure of thin film magnetic recording media using a phase-imaging tapping-mode atomic force microscope (AFM). In this study, clear images obtained with the AFM were compared to those obtained with a transmission electron microscope (TEM). A statistical distribution of grain size was analyzed. This novel method is an important development because phase imaging tapping mode AFM could provide a cheaper and faster characterization alternative to TEM.

Introduction

In order to continue increases in information storage density for personal computers, advanced nanofabrication techniques are being used to produce magnetic media with grain structures in the nanometer size range. The grain size of the media determines important recording properties including aerial density, signal to noise ratio, and thermal stability [1]. In order to successfully fabricate media with nanometer grain size, advanced characterization techniques are required to accurately assess grain sizes.

Because of the nanoscale size of current PMR grains, the TEM has been the tool of choice for grain structure analysis. The TEM provides excellent resolution [2]; however, sample preparation is difficult and time consuming. The AFM can be easily used to image surface topography with little sample preparation. However, to our knowledge, there exist few other efforts using the AFM to analyze nanoscale grain sizes of magnetic thin films [3].

In tapping-mode AFM, an oscillating cantilever scans the sample surface, and tip to sample height is kept constant through the use of an electronic feedback loop. Phase-imaging is an extension of tapping-mode, which measures the contrast in the phase angle between the driving and response frequencies. This data is gathered simultaneously with topographic data. The difference in phase angle is sensitive to several material properties including composition, viscoelasticity and surface adhesion [4]. This data may be used to enhance grain boundary resolution [3]. In this study, we present grain size distributions of PMR media obtained using phase-imaging tapping-mode AFM for the first time.

Experimental Procedure

Two discs of CoPtCr-O PMR with different grain size were analyzed. Samples were etched for 2 minutes in an oxygen plasma to remove a 5 nm protective diamond-like carbon (DLC) layer on the surface of the media and to improve imaging response. A Digital Instruments multimode scanning probe microscope operating in tapping mode was used to characterize the samples both before and after the plasma etch process. Silicon nitride cantilevers with a resonant frequency

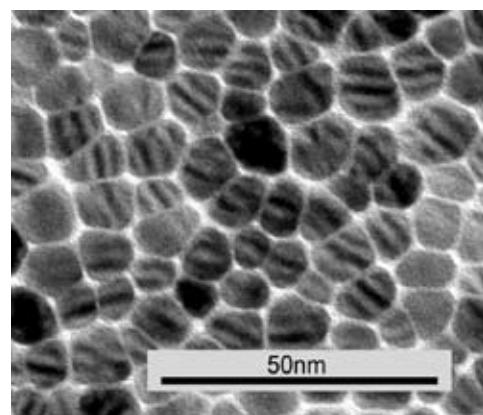


Figure 1: Bright field TEM image of PMR media with 9 nm grain size.

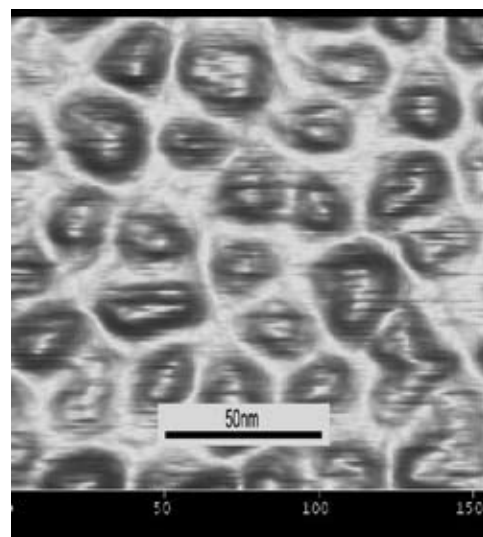


Figure 2: Phase-image tapping mode AFM scan of PMR media with 20 nm grain size.

between 285-315 kHz, and a tip radius of curvature (ROC) of 10 nm were used. TEM images of the samples were obtained before etching. Grain size was determined by taking the average of the large diameter and small diameter of a single grain, with a sample size of 30 grains used for statistical analysis.

Results and Conclusions

In Figure 1, we present a TEM image of a PMR media sample with 9 nm grain size. We compare this with Figure 2, which is an AFM phase image of a different sample of PMR media, having a measured grain size of approximately 20 nm. Note in both images, the individual grains and grains boundaries are clearly visible.

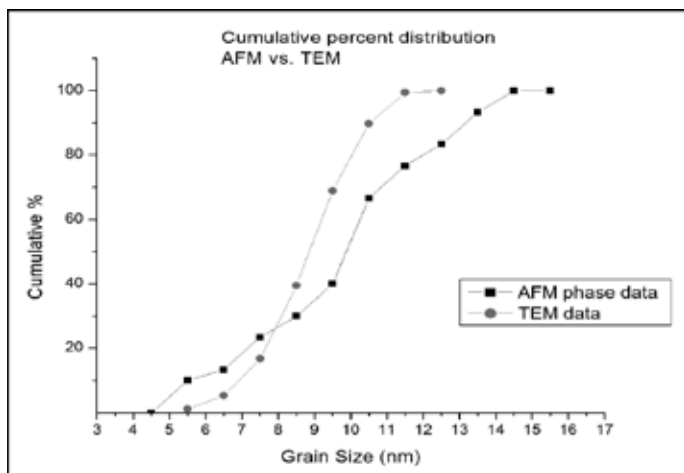


Figure 3: Cumulative percentage plot of grain sizes obtained by TEM and AFM methods.

In Figure 3, we present the measured grain size data for the sample with 9 nm average grain size in a cumulative percentage frequency plot, which has been shown to give reasonable grain size distributions even with small grain size populations [5]. The AFM method yielded slightly larger grain sizes than the TEM method. This may have been because the radius of curvature (ROC) of the AFM tip, at approximately 10 nm, approached the measured grain size and became a limiting factor in the resolution of the scans. In fact, the AFM phase image data agreed quite well with the TEM data as the calibration error of the AFM is approximately 10%.

In Figure 4, we compare the grain size distributions for the 20 nm grain size sample obtained with the AFM topography method and the phase image method. The phase image data was gathered before the sample was etched. This shows the phase difference is sensitive enough to be detected through the 5 nm amorphous DLC layer.

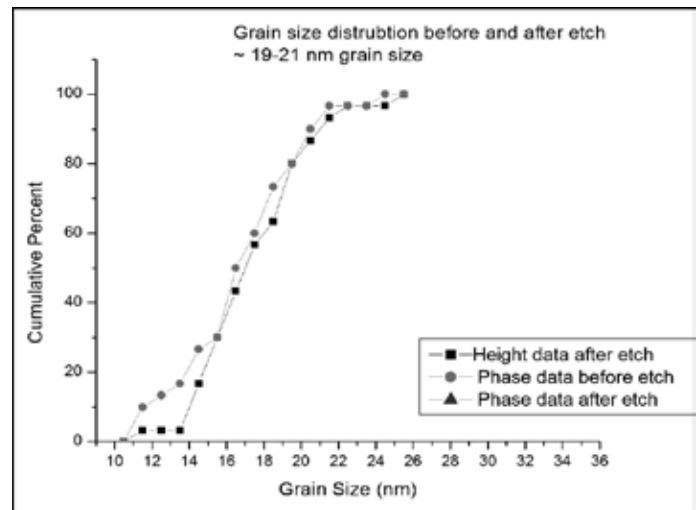


Figure 4: Cumulative percentage plot of grain sizes obtained from AFM height data, and AFM phase-image data.

In this study, we have presented the first images of PMR nanoscale grain structure captured using phase imaging tapping-mode AFM. These are found to compare to TEM nanographs. This work demonstrates that tapping mode AFM can be used for reasonably accurate grain size analysis of magnetic recording media.

Acknowledgements

Sinclair Group, Dave Gage, Dr. Jim Kruger, Mike Deal, Maureen Baran, REU Staff, NNIN REU Program, support from NSF and Center for Integrated Systems.

References

- [1] Piramanayagam, S. N.; "Perpendicular recording media for hard disk drives"; *Journal of Applied Physics*, 102, 11301-11323 (2002).
- [2] Risner, J.; "Transmission electron microscopy analysis of computer hard disc, magnetic thin films"; *Materials Chemistry and Physics*, 81, 241-143 (2003).
- [3] Pang, C.H.; "Application of phase-imaging tapping-mode atomic-force microscopy to investigate the grain growth and surface morphology of TiSi₂"; *Journal of Vacuum Science and Technology B*, 20, 1866-1869 (2002).
- [4] Bhushan, B.; "Phase contrast imaging of nanocomposites and molecularly thick lubricant films in magnetic media"; *Nanotechnology*, 14, 886-895 (2003).
- [5] Park, D.W. and Sinclair, R.; "Grain size analysis of longitudinal thin film media"; *Journal of Applied Physics*, 87, 5687-5689 (2000).

Optical Characterization of Nanostructured Wide Bandgap Semiconductors for Energy Applications

Jessica Smith

Physics and Mathematics, Austin College

NNIN REU Site: Michigan Nanofabrication Facility, The University of Michigan Ann Arbor

NNIN REU Principal Investigator: Professor Pei-Cheng Ku, Electrical Engineering & Computer Science, University of Michigan

NNIN REU Mentors: Min Kim and Luke Lee, Electrical Engineering and Computer Science, University of Michigan

Contact: jsmith@austincollege.edu, peicheng@umich.edu, minwkim@umich.edu, leelk@umich.edu

Abstract

Illumination applications for light emitting diodes (LED's) have been increasing. Therefore, LED's are the dominant focus in the field of solid state lighting. The issue concerning lighting today is the trade-off occurring between high efficiency and high color rendering capabilities. For high efficiency, a white light can be constructed using blue and yellow components. However, to render the color faithfully, the white light must contain at least the primary components blue, green, and red. We explored improving color rendering in a highly efficient dichromatic system.

Introduction

To increase the color rendering index of the dichromatic white light, we broadened the spectral line widths of light emitted at blue and yellow to cover also the green and red components. To prove this concept, we used the selective area epitaxy (SAE) technique for growing indium gallium nitride quantum wells (InGaN QWs). Our methods included changing the pattern of the dielectric mask including pitch and area, and changing the indium incorporation and growth rate of InGaN QWs in different areas to achieve a broader linewidth. To characterize variations of emission wavelengths on the pattern, we used micro-photoluminescence (PL) to locally concentrate high energy. We plan to stack blue and yellow QWs on one LED, and characterize the color rendering index and efficiency of the proposed LED.

When having two layers of GaN separated by a layer of InGaN, a QW forms. Because electrons can occupy a lower energy state in InGaN than GaN, excited electrons tend to go to lower energy states in the InGaN layer. The QW increases the probability of electrons recombining with holes. When electrons and holes recombine, photons are emitted.

Previous results revealed linewidth broadening at blue emission using SAE. To further prove our concept in attaining high color rendering index dichromatic white light, we increased the wavelength to green/yellow. This was achieved by increasing the indium composition of the material to create a different lattice for emitting light and increasing the QW thickness to lower the energy of the photon released. To broaden the emission linewidth, we varied the growth rate of the QW across the wafer by SAE, in turn creating varying QW thicknesses. We adjusted the conditions affecting the concentration gradient that the molecules form, and altered the pattern at which our QWs grew.

The pattern had multiple sites that included different shapes and densities to have different QW thicknesses that emit slightly different wavelengths of light at each site, thus the one LED will have a broader spectrum of emission.

Experimental Process

To define the pattern for SAE, we deposited a layer of silicon dioxide (SiO₂) then a layer of S1805 resist on a GaN template. We used photolithography to expose selected areas of resist to UV light. Then we developed those certain areas by removing the exposed resist with MF AZ 300. Finally, we etched those certain areas into the SiO₂ with a solution of BHF and water.

For QW growth, we used metal-organic chemical vapor deposition. The product that forms when the gas phases of indium and gallium, both attached to an organic molecule when added to ammonia, is InGaN. When incorporating the indium, we used ~ In_{0.2}Ga_{0.8}N. The concentration gradient of the molecules was increased/decreased and the pattern was altered, each partially determining how fast the molecules reached the exposed GaN template. Since the materials always wants to grow at the most stable planes in SAE, the GaN oriented in a hexagonal pyramidal shape.

For micro-PL, we arranged a beam splitter, UV objective lens, as well as other lenses and mirrors to concentrate the UV light onto one micro-pyramid and measure variations of the wavelength emitted from site to site on the pattern. We used the spectrometer to read the spectrum emission.

Results and Conclusions

With the planar QW results, we obtained an InGaN peak at about 510 nm, with the GaN peak at a less intensity. The micro-pyramid QWs were obtained using the same recipe as the planar QWs; however, the micro-pyramid InGaN signal was low as shown in Figure 1. Unfortunately we were not able to obtain micro-PL signal from individual micro-pyramids, possibly due to the weak signal. (Micro-pyramid growth at the $\sim 10 \mu\text{m}$ site is shown in Figure 2. The SEM was under maintenance at the time of measurement.) We also cannot know how the QW thickness and indium incorporation separately affected the wavelength emitted, since both together must be qualities of the QW.

With further testing of possible causes for unattainable micro-PL measurements, we can detect if there is a problem with laser alignment on a micro-pyramid or sample defects. One possible cause could be due to the micro-PL setup. We used a UV objective lens that is coated for light in the non-visible wavelength range, thus the lens was not ideal for light in the green wavelength range when the signal is weak.

Nonetheless, we have proven it is possible to get green emission from micro-pyramid QWs in our PL measurements. Once we have increased the wavelength of light emission and characterized the light produced by measuring each site of our pattern, then we will stack blue and yellow QWs accordingly to improve efficiency. Finally, we will have one LED, and with anticipation the LED will have improved color rendering properties and efficiency.

Acknowledgements

This work was performed in part at the Michigan Nanofabrication Facility, a member of the National Nanotechnology Infrastructure Network Research Experience for Undergraduates Program, which is supported by the National Science Foundation. Thank you to Dr. Sandrine Martin and Prof. Pei-Cheng Ku, along with his research group.

References

- [1] Schubert, E. Fred (2006). "Light Emitting Diodes (2nd ed.)." New York: Cambridge University Press.
- [2] H. Yu, T. Jung, L. Lee, and P. C. Ku, "Multiple Wavelength Emission from Semipolar InGaN/GaN Quantum Wells Selectively Grown by MOCVD," Conference of Laser and Electro-Optics, Baltimore, MD (2007).

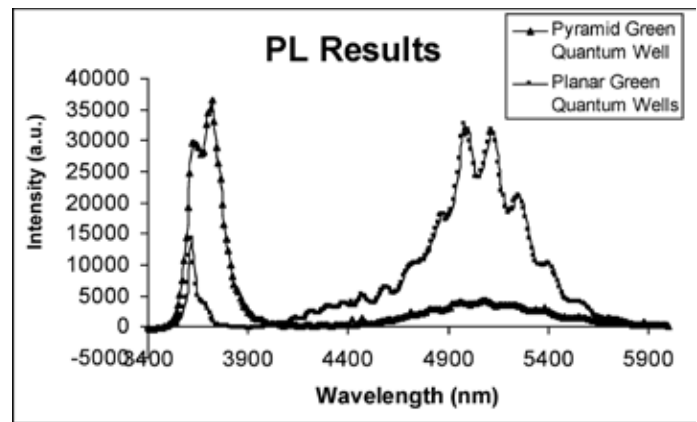


Figure 1: Compared photoluminescence results of planar and micro-pyramid quantum wells.

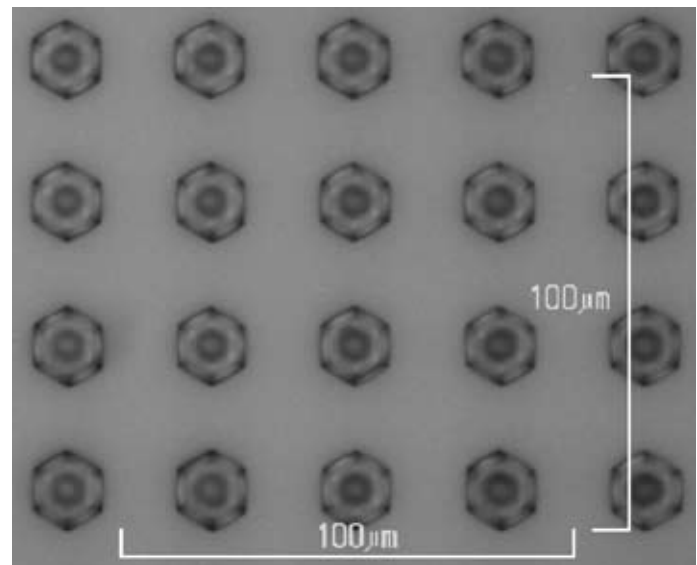


Figure 2: $\sim 10 \mu\text{m}$ diameter array of micro-pyramids.

Investigation of TMAH Release of Stretchable Silicon Networks

Allison Solanki

Physics, Whitman College

NNIN REU Site: Stanford Nanofabrication Facility, Stanford University

NNIN REU Principal Investigator: Prof. Peter Peumans, Electrical Engineering, Stanford University

NNIN REU Mentor: Kevin Huang, Electrical Engineering, Stanford University

Contact: solankak@whitman.edu, ppeumans@stanford.edu, kevhuang@stanford.edu

Abstract

The development of stretchable silicon networks is an important step to realizing cost-effective large area electronics. Devices were fabricated using conventional complementary metal oxide semiconductor (CMOS) processing on wafers which were etched into networks of nodes connected by spiral springs and then stretched to desired size and shape. This investigation focused on developing an approach to release these networks following deep reactive ion etching using a tetramethylammonium hydroxide (TMAH) etch on $\langle 111 \rangle$ wafers. To achieve effective release of these networks, etching parameters such as etch time and temperature of etchant bath were varied until optimal process parameters such as etch rate and oxide selectivity were determined. The ability to successfully create a device on a standard 4" silicon wafer and stretch it to a size ten times or larger is important in the implementation of many large area electronics applications, such as structural health monitoring sensors and solar cells.

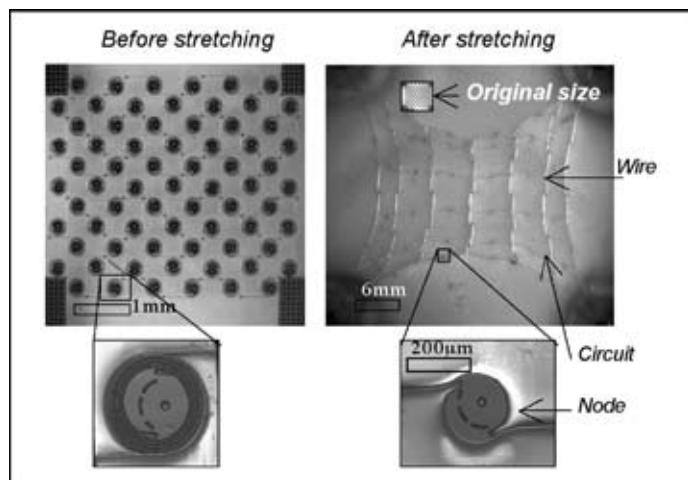


Figure 1: Stretchable silicon network before and after stretching.

Introduction

This research investigated a cost-reducing, consumption friendly fabrication process to release two-dimensional stretchable silicon structures. Eventually, devices or sensors will be placed on individual nodes, in which the spiral springs serve as built-in circuit interconnects for creation of an integrated, robust system as shown in Figure 1.

Previously, stretchable silicon network fabrication required using silicon on insulator (SOI) wafers and employed the xenon difluoride (XeF_2) isotropic dry etch process to release the devices from the substrates. This process was expensive due to the cost of the SOI wafers and inability to reuse the wafers following a single process run. In addition, it was prone to structural problems stemming from pinhole defects particularly in the sidewalls. In response to these consequences, a new wet etch process was employed.

TMAH is a well known non-toxic, anisotropic wet etch solution that was chosen for its ability to etch specific crystal planes at specific rates, its high selectivity to oxide, and for its compatibility with the CMOS process as it does not contain harmful alkali ions [1]. Because TMAH etches the $\langle 111 \rangle$ plane at the slowest rate, it can act as an etch stop much like the buried oxide does in the SOI wafer when bulk Si $\langle 111 \rangle$ wafers are used.

Device Fabrication

The substrates for this investigation consisted of 4" diameter, $\langle 111 \rangle$ oriented Si wafers which were selected for their compatibility with the TMAH target etch planes. The device fabrication process started with the blanket deposition of a $1.6 \mu\text{m}$ thick layer of silicon oxide via low pressure chemical vapor deposition (LPCVD). Next, standard photolithography steps were performed. A dry fluorine etch was subsequently used to etch the exposed network pattern in the oxide. Si was then etched using the Bosch deep reactive ion etch (DRIE) process which consisted of an alternating sulfur hexafluoride (SF_6) etch process and a deposition of octafluorocyclobutane (C_4F_8), which served as a protective passivation layer over the etched structures to create a smooth sidewall.

Next, a $2 \mu\text{m}$ layer of oxide was blanket deposited using LPCVD. A second oxide etch removed the bottom layer of oxide, preparing the wafer for another DRIE. This prepared the Si wafer for the wet etch release. Figure 2 shows the resulting device structure following the second DRIE step. Finally the wafers were subjected to a TMAH bath heated over a hotplate to ensure thorough undercutting of the nodes, spirals, and pads. The bath was closely monitored to ensure a constant temperature and the solution was agitated to help decrease the quantity of hydrogen bubbles, which can disrupt the etching process.

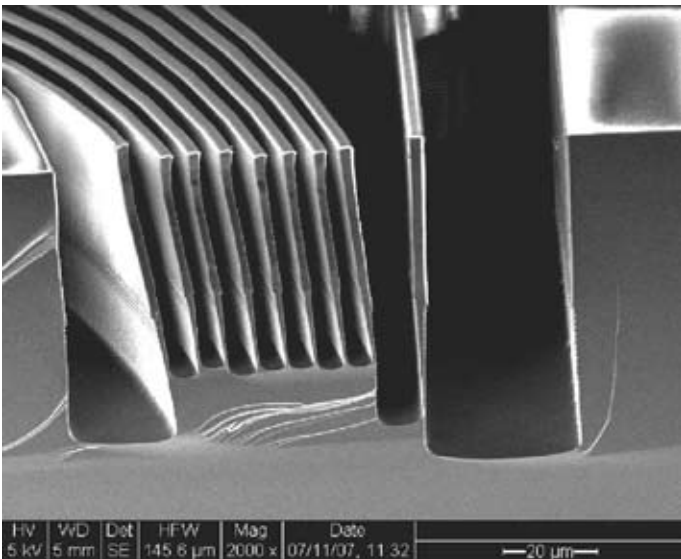


Figure 2: Cross-section of device prior to TMAH wet etch.

Results and Conclusions

Complete structure fabrication was achieved in a clean room environment, and optimal production specifications were determined to successfully release the Si structures from the wafer.

It is well known that planar etch rates are inversely related to the TMAH concentration, thus for optimum results, a 5% TMAH: 95% water bath ratio was used at a temperature of 90°C [2]. With an optimum etch rate of 1.4 $\mu\text{m}/\text{min}$ in the $\langle 110 \rangle$ plane, the TMAH etch process time was determined to be 80 minutes to effectively undercut the silicon nodes, interconnects, and pads. However, transferring the networks between liquid and gaseous states proved difficult.

Traditionally, critical point dryers (CPD) are used to reduce the negative consequences of surface tension. However, the stretchable Si structures are delicate, hence they became easily

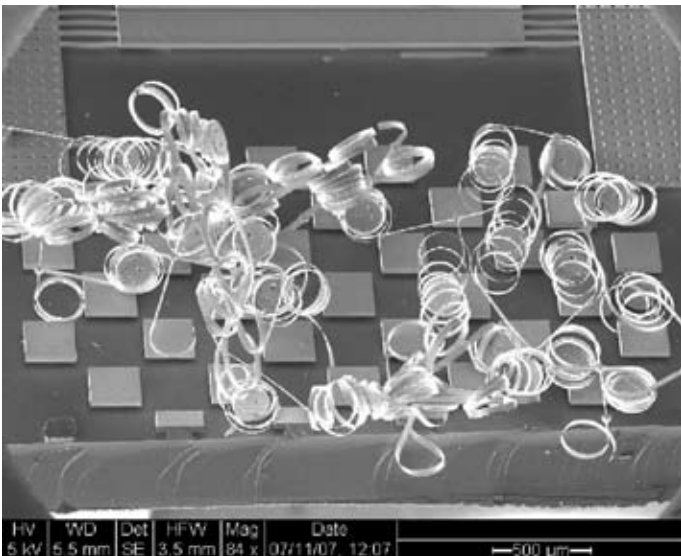


Figure 3: Tangled node network following TMAH etch.

entangled due to the gas flow in the dryer, as shown in Figure 3. This prompted a new investigation directed at successful removal of the structures following the TMAH bath. One solution was found by increasing the distance between the released structure and the substrate during the final DRIE step, followed by air drying the samples after release. Although the substrates still had to be removed from the TMAH solution and thus were subject to some tangling, the networks were nevertheless released without being introduced to the CPD.

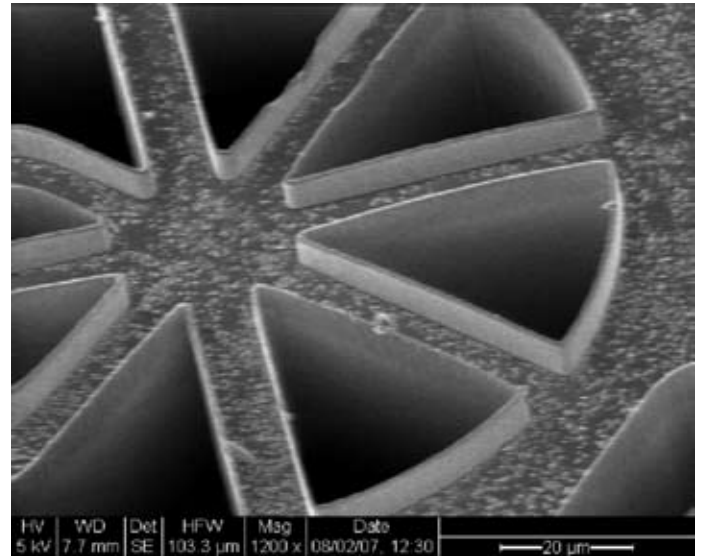


Figure 4: Underside of node showing clean release.

Figure 4 shows a cleanly released node structure. Future work will involve improving this release mechanism. However, we have shown that a cost-effective method to fabricate stretchable silicon networks is viable and important in the implementation of various sensor devices.

Acknowledgements

The author would like to thank Kevin Huang and Dr. Peter Peumans for their guidance and support throughout this research, the Stanford Nanofabrication Laboratory staff, and Dr. Michael Deal and the Stanford Research Experience for Undergraduates program. This work was supported by the Stanford Center for Integrated Systems, the National Nanotechnology Infrastructure Network Research Experience for Undergraduates and the National Science Foundation.

References

- [1] Tsaur, J., et. al. "Development of TMAH Anisotropic Etching Manufacturing Process for MEMS". *Micromachining and Microfabrication Process Technology VI*, Proceedings of SPIE, Vol. 4174, 142-153 (2000).
- [2] Laconte, J., et. al. "Micromachined Thin-Film Sensors for SOI-CMOS Co-Integration". New York: Springer, 2006. p. 17-46.